OPTICAL AND ELECTRICAL DESIGN GUIDELINES OF NANOSTRUCTURED CDTE SOLAR CELLS

A THESIS SUBMITTED TO
THE GRADUATE SCHOOL OF NATURAL AND APPLIED SCIENCES
OF
MIDDLE EAST TECHNICAL UNIVERSITY

BY

CAN ÖZCAN

IN PARTIAL FULFILLMENT OF THE REQUIREMENTS
FOR
THE DEGREE OF MASTER OF SCIENCE
IN
ELECTRICAL AND ELECTRONICS ENGINEERING

SEPTEMBER 2018

Approval of the thesis:

OPTICAL AND ELECTRICAL DESIGN GUIDELINES OF NANOSTRUCTURED CDTE SOLAR CELLS

submitted by **CAN ÖZCAN** in partial fulfillment of the requirements for the degree of **Master of Science in Electrical and Electronics Engineering Department, Middle East Technical University** by,

Prof. Dr. Halil Kalıpçılar
Dean, Graduate School of **Natural and Applied Sciences** ____________

Prof. Dr. Tolga Çiloğlu
Head of Department, **Electrical and Electronics Eng.** ____________

Asst. Prof. Selçuk Yerci
Supervisor, **Electrical and Electronics Eng. Dept., METU** ____________

Examining Committee Members:

Assoc. Prof. Dr. Özgür Ergül
Electrical and Electronics Engineering Dept., METU ____________

Asst. Prof. Dr. Selçuk Yerci
Electrical and Electronics Engineering Dept., METU ____________

Assoc. Prof. Dr. Barış Bayram
Electrical and Electronics Engineering Dept., METU ____________

Prof. Dr. Hüsnü Emrah Ünalan
Metallurgical and Materials Engineering Dept., METU ____________

Asst. Prof. Dr. Serap Aksu
Physics Dept., Koç University ____________

Date: 05.09.2018

I hereby declare that all information in this document has been obtained and presented in accordance with academic rules and ethical conduct. I also declare that, as required by these rules and conduct, I have fully cited and referenced all material and results that are not original to this work.

Name, Last name : Can, Özcan

Signature :

ABSTRACT

OPTICAL AND ELECTRICAL DESIGN GUIDELINES OF NANOSTRUCTURED CDTE SOLAR CELLS

Özcan, Can
MSc., Department of Electrical and Electronics Engineering
Supervisor : Asst. Prof. Selçuk Yerci

September 2018, 69 pages

Cadmium Telluride (CdTe) is a direct band gap material with an almost optimum band gap of 1.5 eV and has a high absorption coefficient at its band edge (>10^4 cm^{-1}). In the last decade, an alternative to the conventional planar structure of CdTe solar cells has been realized by coating the CdTe absorber around ZnO nanorods (NRs). The NRs serve as the front contact of the solar cells with radial charge collection and vertical light absorption at the same time, allowing efficient charge collection and enhanced light trapping properties. Prior to CdTe coating, a thin conformal interfacial CdS layer is usually deposited around NRs which provides a graded band alignment between CdTe and ZnO and passivation of CdTe surfaces. In the NR-based solar cells, the ZnO NR dimension, CdTe and CdS thicknesses, material and interfacial qualities (i.e doping density and surface recombination velocities) are determining factors in the optical absorption and charge collection. In this context, the effects of length, density and angular deviation of the NRs are analyzed through optical and electrical simulations for two types of CdTe solar cell structures, namely the extremely thin absorber (ETA) and buried. Optical simulations are validated in comparison with the experimental haze measurements of CdS/ZnO NRs. While ETA CdTe solar cell uses a thin (~40 nm) absorbing layer around CdS-coated ZnO NRs, CdTe fills the space between CdS-coated ZnO NRs in the buried solar cells. The short circuit current densities are calculated at various CdTe doping densities and CdS/CdTe surface recombination velocities by electrical simulations, and are compared to the conventional planar CdTe solar cells. It was shown that with a moderate doping density of 10^{16} cm^{-3} and relatively high CdS/CdTe surface recombination velocities of 10^4 cm/s, NR-based CdTe solar cells can outperform their planar counterpart by achieving J_{sc} values as high as 27 mA/cm^2. Characterization of CdTe thin films by secondary ion mass spectroscopy, Raman spectroscopies and scanning electron microscope demonstrates that doping densities required to boost the efficiency of NR-based CdTe solar cells can be achieved experimentally. Finally, measured solar cell efficiency of buried structures are also presented.

Keywords: CdTe solar cells, ZnO Nanorods, Light Trapping, CdTe characterization

ÖZ

NANOYAPILI CDTE GÜNEŞ HÜCRELERİ İÇİN OPTİK VE ELEKTRİKSEL TASARIM KILAVUZU

Özcan, Can
Yüksek Lisans, Elektrik ve Elektronik Mühendisliği
Tez Yöneticisi : Dr. Öğr. Üy. Selçuk Yerci

Eylül 2018, 69 sayfa

Kadmiyum Tellür (CdTe) ideal olan 1.5 eV bant aralığı ve bant kenarındaki yüksek soğurma katsayısı (>10^4 cm^{-1}) ile direkt bant yapılı bir malzemedir. Son on yılda geleneksel düzlemsel yapıdaki CdTe güneş hücrelerine alternatif olarak ZnO nanoçubukların (NR) etrafının yüksek soğurmaya sahip CdTe ile kaplanmasıyla CdTe güneş hücreleri üretilmiştir. Nanoçubuklar ön kontakt rolü üstlenmesinin yanısıra radyal yük toplaması ve gelişmiş ışık hapsetme özelliklerine sahiptir. CdTe kaplanmasından önce kademeli bant yapısı sağladığı ve CdTe yüzeyini pasive ettiği için genellikle ince bir CdS tabakası nanoçubukların etrafına kaplanır. Nanoçubuk tabanlı CdTe güneş hücrelerinde ZnO nanoçubuk boyutları, CdTe ve CdS kalınlıkları, malzeme ve arayüz kalitesi (katkılama yoğunluğu ve arayüz rekombinasyon hızları) optik soğurmayı ve yük toplamayı etkileyen faktörlerdir. Bu amaçla nanoçubukların uzunluk, yoğunluk ve açısal sapmaları optik ve elektriksel simülasyonlarla aşırı ince soğurucu (ETA) ve gömülü hücre yapısı olarak adlandırılan iki farklı CdTe güneş hücresi yapısı için analiz edilmiştir. Deneysel verilerle karşılaştırma yapılarak ZnO/CdS nanoçubukların ışık saçma miktarlarının optic benzetimlerle doğru bulunduğu gösterilmiştir. ETA CdTe güneş hücreleri, CdS kaplı nanoçubukların etrafına kaplanan ince bir CdTe tabakası (~40 nm) kullanırken, gömülü CdTe güneş hücrelerinde CdTe malzemesi CdS kaplı ZnO nanoçubukların arasındaki boşlukları doldurmaktadır. Kısa devre akım yoğunlukları elektriksel benzetimlerle farklı katkılama yoğunlukları ve CdS/CdTe yüzey rekombinasyon hızları için hesaplanmış ve geleneksel düzlemsel CdTe güneş hücreleriyle karşılaştırılmıştır. Benzetim sonuçlarından görülmüştür ki, 10^{16} cm^{-3} seviyede katkılanan ve yüksek bir CdS/CdTe yüzey rekombinasyon hızı olan 10^{4} cm/s ile 27mA/cm^{2} J_{sc} değerine ulaşılarak düzlemsel güneş hücrelerinden daha yüksek J_{sc} elde edilmiştir. İkincil iyon kütle specktroskopisi, Raman spektroskopisi ve taramalı elektron mikroskobuyla karakterize edilen CdTe düzlemsel örneklerin benzetimlerde gösterilen katkılama yoğunluklarına ulaşabildiğini deneysel olarak göstermiştir. Son olarak, gömülü CdTe güneş hücrelerinin verimlilik ölçümleri sunulmuştur.

Anahtar Kelimeler: CdTe güneş hücreleri, ZnO nanoçubuklar, ışık hapsetme, CdTe karakterizasyonu

ACKNOWLEDGMENTS

I wish to express my gratitude to Asst. Prof. Dr. Selçuk Yerci for his constant support and guidance during my Master's study. Working under his supervision has improved me as a researcher much more than I could have imagined.

My sincere thanks go to the members of Advanced Photonics and Photovoltaics group for all the technical discussions we had and the fun we shared during my studies, especially to Arman Ayan, Cem Şahiner, Wiria Soltanpoor, Hava Akpınar, Esra Bağ, Mehmet Koç, Milad Ghasemi and Çağıl Köroğlu.

I want to thank Deniz Türkay for his technical help on the electrical simulations. A lot of ideas were born during the discussions we held.

I would also express my gratefulness to Dr. Giray Kartopu for providing CdTe samples for material characterization and his guidance during this study.

My sincere thanks go to Wisnu Hadibrata, who has not only been a great lab mate but also initialized the ideas for optical simulations.

I would like to thank to Sedat Canlı for the scanning electron microscopy images and to Binnur Özkan for Raman spectroscopy measurements at METU central laboratory.

I have to express my biggest gratitude to my soon-to-be wife Esra Kaymak, without her support this thesis would have been much more difficult to accomplish. I feel blessed with all the patience and support she has given me during my hard work.

This thesis was supported by the Scientific and Technical Research Council of Turkey (TÜBİTAK) under the contract number 114F518. I would also like to thank TÜBİTAK for 2210 scholarship program as the financial support during my Master's study.

TABLE OF CONTENTS

LIST OF TABLES

LIST OF FIGURES

NOMENCLATURE

A_{CdTe}	Absorption in CdTe
Au	Gold
AM	Air Mass
c	Speed of Light
CdS	Cadmium Sulfide
CdTe	Cadmium Telluride
DOS	Density of States
ETA	Extremely Thin Absorber
ϕ_i	Solar Irradiance
FDTD	Finite-Difference Time-Domain
FWHM	Full width at half maximum
h	Planck’s Constant
ITO	Indium Tin Oxide
J_{sc}	Short Circuit Current Density
λ	Wavelength
MAPC	Maximum Achievable Photocurrent
Mg	Magnesium
MOCVD	Metalorganic Chemical Vapor Deposition
NR	Nanorod
PMMA	Polymethyl Methacrylate
PV	Photovoltaic
q	Elementary Charge
SILAR	Successive Ion Adsorption and Reaction
SIMS	Secondary Ion Mass Spectroscopy
SCR	Space Charge Region
TCO	Transparent Conductive Oxide
ZnO	Zinc Oxide

CHAPTER 1

INTRODUCTION

1.1 Current Status of CdTe Solar Cells

In 2017, the solar cells in the world had a power production capacity of 94.6 GW, generating 1.7 % of the world's electricity. While Silicon solar cells dominated the market by 93.3 % of the total solar cell production, CdTe solar cells follow Si solar cells by a 2.3 % share in the global PV market having constituted more than 50 % of the global thin film PV production in 2017. Besides, CdTe solar cells have the shortest energy pay-back time among industrial solar cells [1].

Shockley-Queisser limit defines the maximum theoretical power conversion efficiency of a solar cell utilizing a single p-n junction for a given band gap [2]. CdTe, with its ~1.5 eV direct band gap, is an almost optimum material for PV as shown the Shockley-Queisser limit with respect to band gap in Fig. 1.1. Additionally, CdTe has a high absorption coefficient near its band edge ($>10^4$ cm^{-1}) making it an excellent material for photovoltaics [3]. Thanks to these properties of CdTe, efficiencies of 22.1 % and 21.0 % have been achieved for CdTe solar cells and modules, respectively [4]. Although the high efficiencies of CdTe are promising for large scale electricity production, Te is a scarce element and its supply is limited. By 2020, the CdTe PV technology is expected to be material constrained due to a large increase in the Te prices, hence, the CdTe amount in the solar cells must be reduced while increasing the efficiencies [5]. For this purpose, the thickness reducing the CdTe layer thickness in solar cells has been studied [6], [7]. These studies demonstrated the feasibility of reducing the CdTe layer thickness below 1 µm, however, the efficiencies of the submicron CdTe layers remained unsatisfactory. As an alternative to these efforts, ZnO nanostructures have been incorporated in CdTe solar cells [8]–[14]. Unlike the direct deposition of planar layers for conventional CdTe solar cells, the nanostructured CdTe solar cells are realized by growing nanostructures and conformally coating the nanostructures with the absorbing CdTe layer.

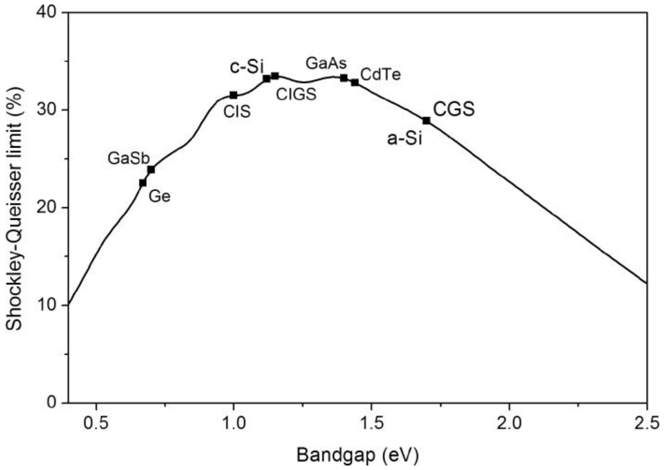

Figure 1.1: Shockley-Queisser limit vs. Bandgap of the material [15]

1.2 Conventional CdTe Solar Cell Structures

Thin film solar cells can be realized by substrate type or superstrate type structures. A typical substrate type CdTe solar cell structure is given in Fig. 1.2.a. In the substrate type structure, the light is incident on the TCO layer on the top of the structure. Then, light travels through the buffer and window layers, typically ZnO and CdS, respectively. The portion of light reaching to the CdTe layer is absorbed. The top and bottom electrical contacts are usually a TCO layer and a metal layer, generally Au, respectively. The substrate type structure is advantageous since it allows utilization of flexible metal foils as the substrate material, leading to roll-to-roll manufacturing with reduced prices [16]. The efficiencies of substrate type CdTe solar cells, however, have been limited [17]–[19] mainly due to the high temperature processes that cause the dopants in CdTe to diffuse into other layers. The diffusion of dopants occurs since the CdTe layer must be deposited on the substrate or flexible metal foils first, followed by the CdS, ZnO and TCO layers, as indicated by the deposition order in Fig. 1.2.a. A study achieved 13.6 % efficiency by coating a Cu layer with a Cu layer thinner than an equivalent thickness less than a monolayer and diffusing Cu into the CdTe layer [16] but the large scale applicability of such a method stands questionable due to long term instability of Cu dopants [20].

The superstrate configuration, shown in Fig. 1.2.b, requires the utilization of a transparent substrate, such as glass. The superstrate is coated with a TCO as a front contact on which the CdS window and ZnO buffer layers are deposited. Following the deposition of these layers, CdTe layer is deposited and with the evaporation of the top metal contact the superstrate CdTe solar cell is completed. The superstrate type CdTe solar cells have been fabricated for almost 50 years [21]. The deposition order, indicated in Fig. 1.2.b, allows the ZnO buffer and CdS window layers to be unaffected by the diffusive dopants. Considering the large scale applicability of superstrate type CdTe solar cell structure and significantly higher efficiencies than their substrate counterparts [22]–[24], the analysis of solar cells in this thesis is kept limited to superstrate CdTe solar cell configuration.

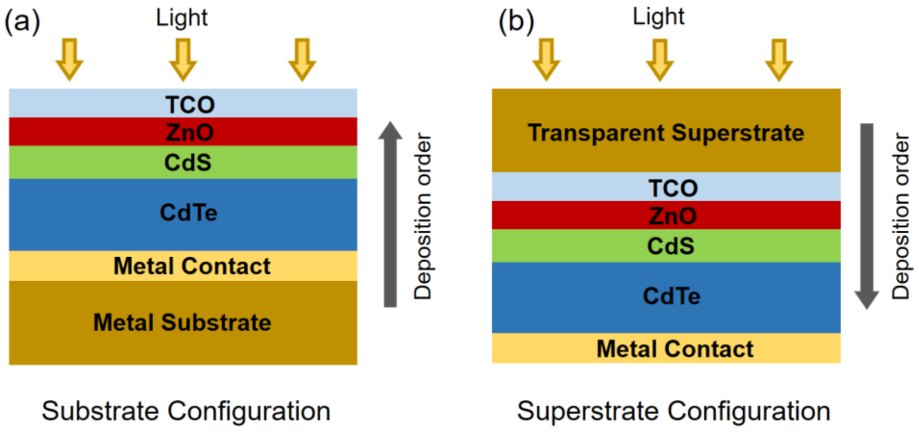

Figure 1.2: The typical (a) substrate and (b) superstrate CdTe solar cell structure

The record power conversion efficiencies of CdTe solar cells achieved with conventional CdTe solar cell structures are given in Fig. 1.3. The record efficiencies of the CdTe solar cells highly increased from years 2011 to 2016 to reach the record efficiency of 22.1 %. These high efficiencies make CdTe a strong candidate for large scale energy production.

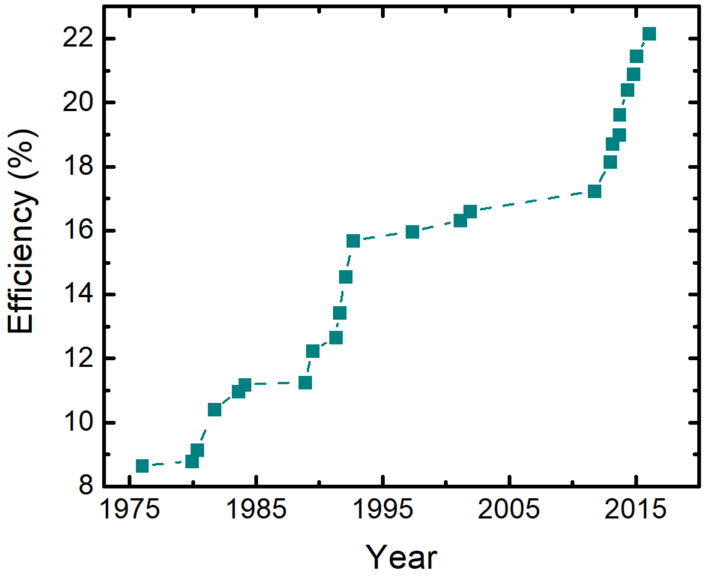

Figure 1.3: The record power conversion efficiency of the CdTe solar cells with respect to year (Data taken from [25])

1.3 Nanostructured CdTe Solar Cells

Sensitizing nanostructures with quantum dots [26], [27] and organic dyes [28] or coating conformal layers of semiconductors around numerous nanostructures [29], [30] have been popular for solar cell applications due to easy and inexpensive device fabrication. For CdTe solar cells, a specific attention has been given to ZnO NRs. Conformal coating of extremely thin absorber (ETA) CdTe layer around randomly oriented NRs has attracted attention in the last 2 decades [8]–[14], [31]–[33]. While planar CdTe layer thicknesses usually exceed 1 µm, the CdTe coating of nanostructures involves CdTe thicknesses ranging from a few nanometers up to hundreds of nanometers. An illustration of ETA CdTe structure with ZnO NRs structure is shown in Fig. 1.4 as an example without the top contact layer for simplification. In such a ZnO NR-based structure, the light travels in the vertical direction in the absorbing CdTe layer. The vertical propagation of light causes increasing absorption in CdTe layer considering the reduced CdTe. The charge collection, on the other hand, occurs radially through the thin CdTe layer, allowing efficient charge collection [34]. Therefore, NR-based CdTe solar cells allow efficient light absorption and charge collection at the same time with reduced CdTe amount in the cell. Additionally, ZnO NRs have been shown to scatter light due to their random orientations [35], [36]. The inherent scattering properties of NRs induce light trapping effect in the solar cell, increasing the absorption of light. The combination of these effects reduces the need for a thick CdTe layer as in the planar CdTe solar cells.

Unlike ETA CdTe solar cells, some NR-based CdTe solar cells employ thicker layers of CdTe, filling the gaps between nanostructures with a buried CdTe layer [13]. The complete burying of the nanostructures increases the CdTe amount in the solar cells compared to the ETA CdTe solar cells but the consumed CdTe amounts are below the conventional planar CdTe solar cell structure. Buried CdTe solar cells exhibit different light trapping and charge collection effects different from that of ETA solar cells due to their bulkier CdTe layer, which will be evident in the following sections.

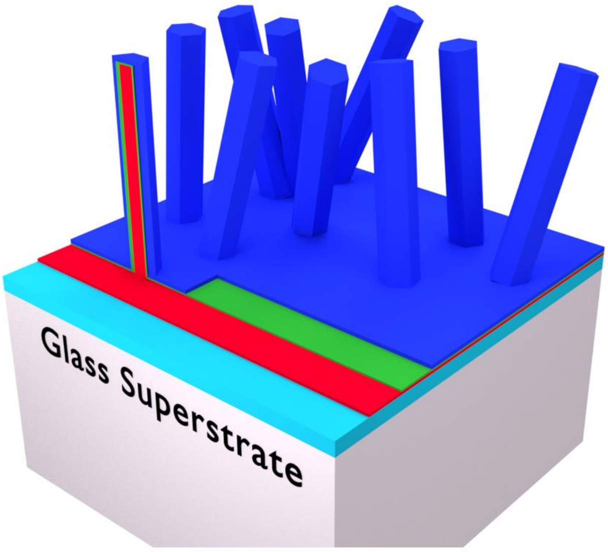

Figure 1.4: ETA CdTe layer (blue) coated around NRs (red) with a thin CdS layer (green) on a TCO layer (cyan)

The efficiencies of some CdTe solar cells incorporating ZnO nanostructures are given in Table 1.1. The efficiencies of both ETA and buried type CdTe solar cells are much lower than the planar CdTe solar cells given in Fig. 1.3. The investigation of the low efficiencies and J_{sc} of nanostructured CdTe solar cells is necessary in this study.

Table 1.1: The type, J_{sc} and efficiencies of various nanostructure based CdTe solar cells

Ref	Substrate	Structure	Type	J_{sc} (mA/cm^2)	η (%)
[8]	FTO/glass	ZnO/CdTe NR	ETA	0.35	0.01
[10]	ITO/glass	ZnO/CdTe NR	ETA	5.9	-
[11]	FTO/glass	ZnO/CdS/CdTe NR	Buried	8	0.7
[12]	FTO/glass	ZnO/CdS/CdTe NR	ETA	4.93	1.05
[13]	ITO/glass	ZnO/CdS/CdTe NR	Buried	15.9	4.2

1.4 Organization of This Thesis

In this thesis, the nanostructured CdTe solar cells are reviewed and the relatively low efficiencies of these solar cells are understood through optical and electrical simulations. Two types of nanostructured solar cell structures, namely the ETA and Buried solar cells, are designed in consideration with the experimental limitations and large scale applicability and the loss mechanism of them are identified through optical and electrical simulations. It is shown that buried CdTe solar cells with 2000 nm-tall ZnO NRs and a moderate doping density of 10^{16} cm^{-3} can achieve a J_{sc} of 28 mA/cm^2. ETA CdTe solar cells with 1000 nm-tall ZnO NRs and doping density of 10^{16} cm^{-3}, on the other hand, can achieve the same J_{sc} with a planar solar cell with 3 times higher CdTe amount. The results are promising on the purpose of reducing the CdTe amount in solar cells while maintaining high efficiencies.

In Chapter 2, the structural parameters of nanostructure based CdTe solar cells reported in the literature are surveyed with the consideration of fabrication techniques. The relatively low efficiencies of these solar cells and the need for exploration of the loss mechanism are addressed. Based on the experimentally-achieved nanostructure geometries and efficiencies, two types of solar cells structures are proposed.

In Chapter 3, the optical properties of the proposed nanostructure based CdTe solar cells are investigated with respect to nanostructure dimensions and solar cell design with optical simulations. The light scattering properties of ZnO NRs are shown with their benefits in solar cells. The parasitic loss mechanisms are revealed and methods compensate for the losses have been offered.

In Chapter 4, the charge collection efficiencies of the optically simulated solar cells are obtained through electrical simulations. J_{sc} of the two solar cell types with various doping densities, surface recombination velocities and nanostructure dimensions are obtained and compared to that of planar CdTe solar cells for comparison. The high recombination losses are explained and suggestions for doping densities and surface recombination velocities are given.

In Chapter 5, brief information about secondary ion mass spectroscopy (SIMS), Raman spectroscopy and scanning electron microscope (SEM) is presented. Planar CdTe layers fabricated on CdZnS/ITO/Glass with different dopant concentrations are characterized with the abovementioned characterization techniques to ensure that simulated nanostructured CdTe solar cells parameters are in coherence with the experimentally achievable material parameters in terms of doping density and its effect on the CdTe material quality. Then, J-V curves of a NR-based CdTe solar cell is presented and its efficiency is analyzed and compared with a planar CdTe solar cell.

CHAPTER 2

STRUCTURAL DESIGN OF NANOSTRUCTURED SOLAR CELLS

2.1 Review of ZnO Nanostructures for Solar Cells

ZnO is a wide band gap semiconductor (3.37 eV) with high electron mobility and relatively easy crystallization properties [37]. Although the CdS/CdTe solar cells originally did not utilize ZnO layers, adapting a thin ZnO buffer layer reduces shunts caused by the pinholes in CdS [38] and increases the charge collection performance due to enhanced electron selectivity. Variety of one-dimensional single-crystal ZnO nanostructures have been fabricated such as nanorods [39], nanobelts [40], nanotubes [41], nanorings [42] and complex hierarchical structures [43]. NRs have attracted attention in particular due to its ease of fabrication and enhanced charge collection and light trapping effects in solar cells.

Despite the light trapping and radial charge collection properties of ZnO NRs, the solar cells with ZnO/CdTe NR arrays performed with efficiencies lower than 1 %. Some studies indicated that insertion of a thin CdS interfacial layer between ZnO and CdTe layers increased the efficiencies of these solar cells due to the graded band alignment and reduced defect density at the interfaces [11], [12]. Even with the insertion of the CdS interfacial layer, the nanostructure-based CdTe solar cells still performed lower than their planar counterparts [11]–[14]. The low performance of ZnO NR-based CdTe solar cells requires a thorough understanding of optical and electrical loss mechanism in the solar cell structure. While the optical and electrical design of planar solar cells is fairly straightforward thanks to their simple structures, optical and electrical modeling of nanostructured solar cells are difficult due to complex and random device structure. The calculation of light propagation and absorption in the solar cell structure as well as the modelling of charge collection, bulk and interface losses are complicated for nanostructured CdTe solar cells. To reduce the complication, the nanostructure-based solar cell structures were designed based on the already-achieved solar cell geometries and material properties. The following subsections consider the nanostructure-based CdTe solar cells in the literature and two design for CdTe solar cells are proposed in section 2.5.

ZnO NRs are usually grown by hydrothermal growth [11]–[13], [39], electrochemical growth [10], [14] and chemical bath deposition [44] on a ZnO seed layer, glass or transparent conductive oxides. The scanning electron microscope images presented in some studies [10]–[13], [39], [44] were analyzed to obtain the NR heights, densities, diameters and angular deviations of the NRs. 4 of the investigated The obtained NR parameters are summarized in Table 2.1. ZnO NRs with 500-2000 nm height, 80 nm diameter, angular deviations ranging from 0 to 20 degrees and densities ranging from 5 to 50 rods/µm^2 were found suitable for solar cell analysis.

Table 2.1: ZnO NRs geometrical presented in some studies. The parameters which were extracted from the SEM images are indicated with an asterisk.

Ref.	Diameter (nm)	Height (µm)	Angular dev. (degrees)	Density (rods/µm^2)	ZnO seed layer thickness (nm)
[10]	147	7	~0*	6*	-
[11]	40 – 80	0.36	18*	-	80
[12]	100 - 200	2 - 3	25*	5*	320*
[13]	90*	1.3 – 1.4	12*	58*	16
[39]	~80	0.5 - 4	-		0
[44]	70*	1.5	-	36*	100

2.2 The CdS Window Layer and CdTe Absorber Layer

CdS is a material with 2.4 eV band gap and is used in CdTe solar cells as the window layer between CdTe and ZnO or CdTe and TCO layers. In superstrate CdS/CdTe solar cells, CdS layers are incorporated as the n-type side of the p-n heterojunction. For large scale planar CdTe solar cell production, usually chemical bath deposition is used [17], [45], [46] but the thicknesses of these CdS layers, however, are usually above 80 nm to ensure pinhole-free layers. Considering the high absorption coefficient of CdS below its band gap, shown in Fig. 2.1, the thick CdS can deteriorate the performance of the solar cells at due to the high parasitic absorption in CdS at short wavelengths.

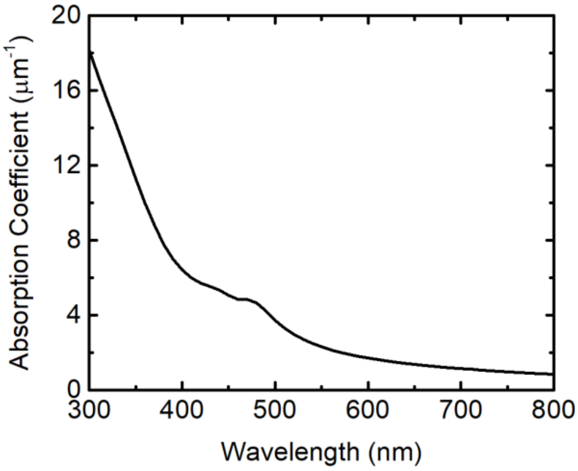

Figure 2.1: The absorption coefficient of CdS (data is taken from [47])

The selection of the thickness and the conformal deposition method of the CdS layer is crucial for device performance for nanostructured CdTe solar cells. Zhang et al. [11] pointed out that a 4 nm-thick CdS layer is enough for passivating ZnO NR surfaces while keeping the parasitic absorption in CdS low. Conformal deposition methods such as successive ionic layer adsorption and reaction (SILAR) [11], electrochemical deposition [12], metalorganic chemical vapor deposition (MOCVD) [13] for the deposition of CdS were used in previous works in which CdS thicknesses ranging from 2 to 20 nm were achieved on ZnO NRs with high conformity. In this study, adapting a 15 nm-thick CdS layer for the formation of solar cell structures was found suitable.

Planar CdTe layers are generally deposited with close-space sublimation [46], but this method is insufficient for conformal coating of CdTe around ZnO/CdS NRs. For NR-based solar cells, the CdTe absorber layer was conformally deposited using electrochemical deposition [10], [12], SILAR [11] and MOCVD [13]. In a study, long deposition periods of CdTe resulted in complete filling of the volume between ZnO/CdS NRs with CdTe achieving an efficiency of 4.5% [13], which is promising for ZnO NR-based CdTe solar cells. The thicknesses of ETA CdTe layers are within the range of tens of nanometers. To be in coherence with the reported CdTe thicknesses, a 40 nm-thick CdTe layer was seen appropriate for this study.

CdTe solar cells' efficiencies were seen to suffer at around 1-5 % unless $CdCl_2$ heat treatment is applied [48]. This treatment is applied in the presence of $CdCl_2$ at temperatures between 350-450 °C for 20-60 minutes. Although the origin of the efficiency enhancement has not been fully understood, the origin is attributed to various factors such as recrystallization and grain growth of CdTe [7], enhancement of charge carrier lifetimes [49] and suppressing the defects in CdS and CdTe layers [50].

The doping of CdTe has been an issue due to the self-compensating effect of As dopants in CdTe due to the formation of AX centers and defect formation with a Cd site or Cd vacancy [51]. While doping densities of 10^{16} cm^{-3} are achievable for CdTe solar cells, doping densities higher than 10^{17} cm^{-3} require excessive attention to the doping process [16] or utilizing a single crystalline CdTe layer [52] which is not practical for large scale CdTe solar cells. The difficulty of doping is taken into consideration for the electrical simulations.

2.3 Proposed CdTe Solar Cells Structures

The nanostructure-based CdTe solar cells were designed in accordance with the analysis on the NR geometries and layer properties. A 30 nm-thick ZnO seed layer was assumed on an ITO/glass superstrate with an ITO thickness of 150 nm. ITO is assumed to be front contact in this structure. In accordance with the chosen ZnO NR geometries, the ZnO NRs were created on a ZnO seed layer. The ZnO NRs were coated with a thin CdS window layer of 15 nm thickness. The resultant ZnO/CdS NRs are illustrated in Fig. 2.2.a.

According to the analysis on CdTe layer, two types of solar cell structures were analyzed, namely the ETA solar cell structure and the buried solar cell structure. ETA solar cell structure were designed with a thin CdTe layer conformally coated around

ZnO/CdS NRs. The conformal CdTe layer thickness in the ETA solar cell structure was chosen as 40 nm. To complete the solar cell structures, the resultant ZnO/CdS/CdTe were partially filled with PMMA and then the remaining gaps between NRs are filled with Au rear contacts. PMMA is a nonconductive and transparent polymer and was used in the ETA solar cell structure to avoid complete filling of the ZnO/CdS/CdTe NRs with Au. A complete Au filling was shown to create plasmonic effects and enhancing the optical losses in the Au layer while partial filling with a polymer was seen to improve the losses, hence, partial filling with PMMA is expected to suppress parasitic absorption in Au. The ratio of PMMA/Au filling was chosen such that at least 90% of the NR tips are in contact with the Au layer. The illustration of the ETA solar cell structure is given in Fig. 2.2.b.

The buried structure was formed with the complete filling of ZnO/CdS NRs with the buried CdTe layer with an excess layer of 100 nm on the tips of NRs corresponding to an overgrowth during CdTe growth. The top of the CdTe layer was coated with 150 nm-thick Au rear contacts and the buried solar cell structure is illustrated in Fig. 2.2.c.

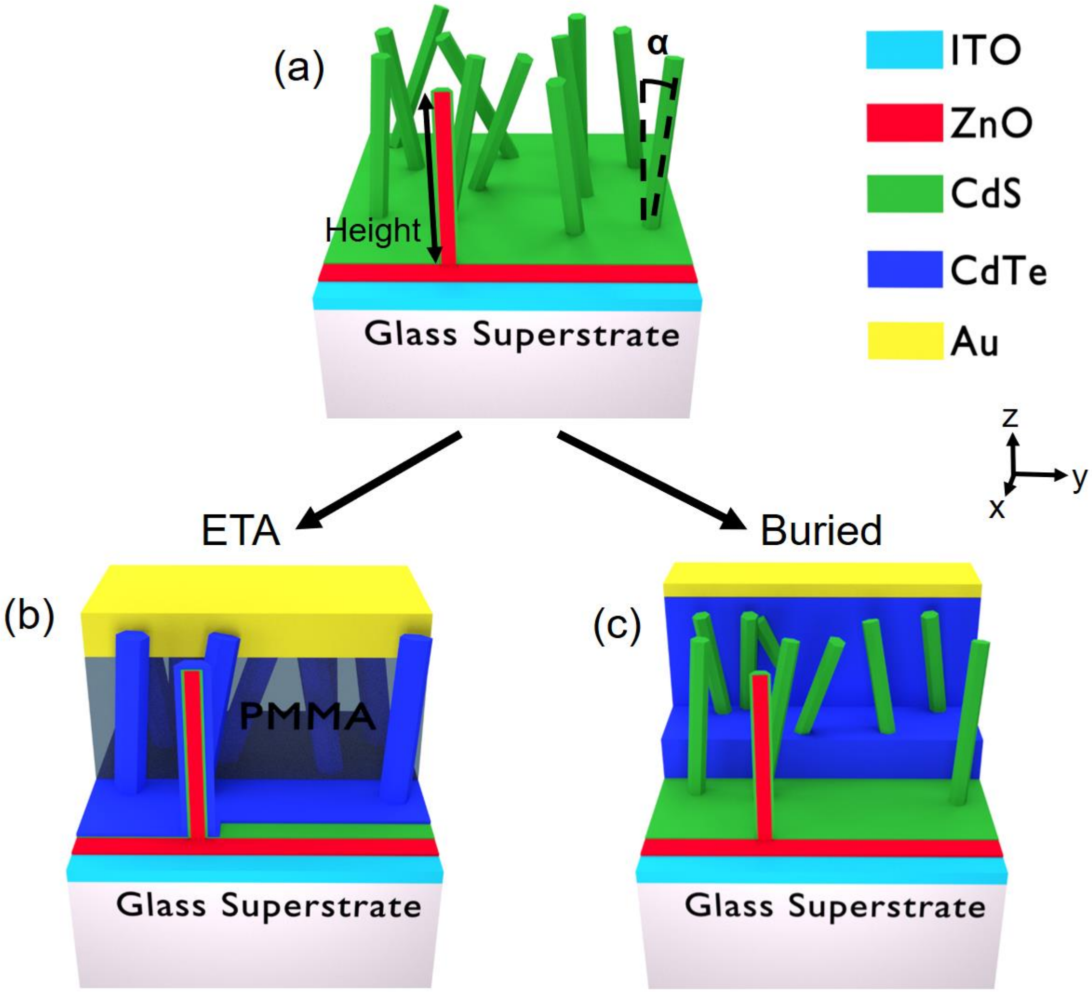

Figure 2.2: (a) ZnO/CdS NRs, (b) ETA solar cell structure and (c) buried solar cell structure

CHAPTER 3

OPTICAL OPTIMIZATION OF NANOSTRUCTURED SOLAR CELLS

3.1 FDTD Simulation Methodology

The optical simulation of nanostructure-based CdTe solar cells was performed with a commercial-grade simulator based on the finite-difference time-domain (FDTD) method (Lumerical, FDTD Solutions). A MATLAB code was used to generate the random positions of the ZnO NRs on the x-y plane and the angular deviation from the z-axis. The random positions of NRs were generated for every individual NR for the desired NR height and density using an algorithm which placed the bases of the NRs at random locations allowing a minimum distance between NRs changing from 90 nm for the densest NRs (corresponding to a NR density of ~50 rods/µm^2) to 380 nm for the least dense NRs (corresponding to a NR density of ~5 rods/µm^2). The angular deviation from the z-axis, denoted by α in Fig. 2.2.a, was also individually and randomly assigned in x- and y-directions assuming a Gaussian distribution with a constant mean of 0 degrees and the standard deviations were swept from 0 to 20 degrees. The standard deviation of the Gaussian distribution is referred to as the angular deviation in the rest of this paper and should not be confused with the mean angle of the Gaussian which is constant 0 degrees.

Size of the simulation domain was chosen as large as 2000 nm to successfully model the large scale light scattering effects of the NRs due to their random orientations. The size of the simulation domain was changed in the z-direction according to the height of the solar cell structure. X- and y-boundaries were chosen as periodic boundary conditions while perfectly matched layers were used at the z-boundaries. A 5 nm uniform cubic mesh sizes were used. A plane wave source was normally incident to the solar cell from the glass with a broad spectral range of 300-

900 nm. A uniform wavelength spacing of 5 nm was used for a highly resolved absorption and haze data. The absorption calculation in each layer of the structures was done by taking 2-D slices from the 3-D structures and averaging the obtained absorption values from the 2-D slices, since calculation of the absorption in the whole 3-D simulation domain would require an excessive amount of memory and processing power. 10 of the 2-D slices were observed to be enough to calculate the absorption in each layer. The photo-generation profiles were calculated by integrating the solar photon flux and absorption in each mesh point in the simulation domain over a wavelength region of 300-850 nm. The volumetric amount of CdTe layers for each geometry were also calculated from the slices taken from the 3-D structure. The material refractive indices were taken from the literature for ITO [53], ZnO [54], CdS [47], CdTe [47], Au [55] and PMMA [56].

Optical simulations were performed in two steps. Firstly, ZnO/CdS NRs on ITO/Glass were simulated for the 27 geometrical configurations (i.e. 3 heights, 3 densities and 3 angular deviations), and the absorption, transmission and haze spectra were extracted. Secondly, the ETA and buried cells were simulated, and the absorption, reflection and optical generation profiles were extracted. The absorption spectra in CdTe is weighted with the solar irradiance to obtain the maximum achievable photocurrent (MAPC) with the given solar cell structure. The standard solar irradiance is AM 1.5G spectrum, whose spectral intensity is given in Fig. 3.1. AM 1.5G spectrum is the solar irradiance after the sun light travels 1.5 atmosphere length before reaching to the solar cell. The 1.5 atmosphere length corresponds to a global tilt of 48.2° from the normal of the ground. The spectral intensity is given in terms of the power falling per unit are per wavelength.

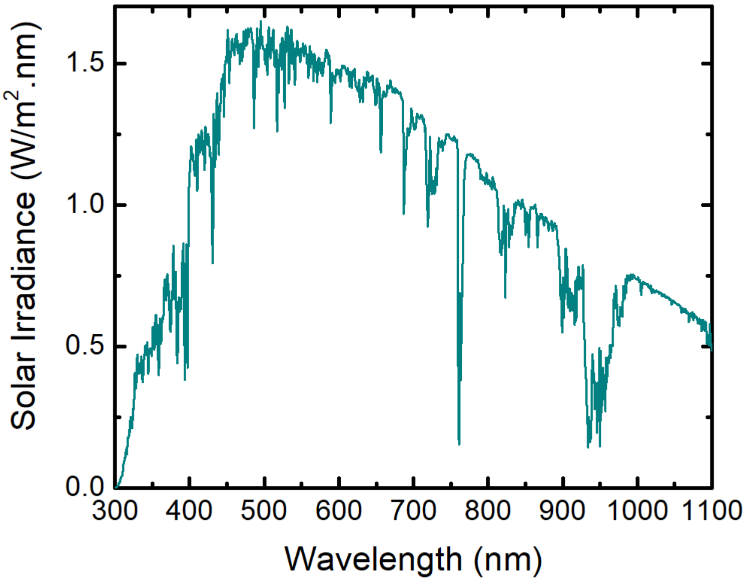

Figure 3.1: AM 1.5G solar irradiance vs. wavelength.

The weighting with the solar irradiance is done by converting the power term of the solar irradiance to the number of photons per second and integrating this value with the absorption in the CdTe layer up to the band gap of CdTe as given in Eq. 3.1

$$MAPC = \frac{q}{h\,.\,c}\cdot\int_{300\,nm}^{850\,nm} \lambda\,.\,A_{CdTe}(\lambda)\,.\,\phi_i\,(\lambda).\,d\lambda \qquad \text{Eq. 3.1}$$

where q is the elementary charge, λ is the wavelength of the incident light, h is the Planck's constant, c is the speed of light, A_{CdTe} is the absorption in CdTe layer and ϕ_i is the AM 1.5G solar spectral irradiance. MAPC is used as the figure-of-merit for optical performance.

3.2 The MAPC Analysis

The MAPC of each configuration of ZnO NRs were found from the absorption in CdTe and the results are given in Fig. 3.2. The MAPC of buried solar cells are higher than that of ETA solar cells for every geometrical configurations of NRs, making them superior in terms of light absorption. MAPC of both ETA and buried solar cells increase with the height of NRs when the angular deviation and density are kept constant. The angular deviation increases the MAPC of the buried solar cells in each geometrical configuration while its effect on ETA solar cells are ambiguous. Contrarily, the effect of NR density on the MAPC of buried solar cells is complicated while the MAPC of ETA solar cells strongly increase with NR density for constant NR height and angular deviation. These trends cannot be directly explained and requires detailed analysis. Although with some NR geometries MAPCs of <27 mA/cm^2 can be achieved, the reduction in the CdTe amount as well as the light trapping properties of ZnO NRs must be thoroughly understood to effectively use the CdTe layers. Besides, the parasitic absorption needs to be known to realize the limitations of the geometrical configurations. For this purpose, the haze analysis, equivalent CdTe thickness analysis, parasitic absorption analysis and interference effect analysis have been performed and given in the following sub-chapters.

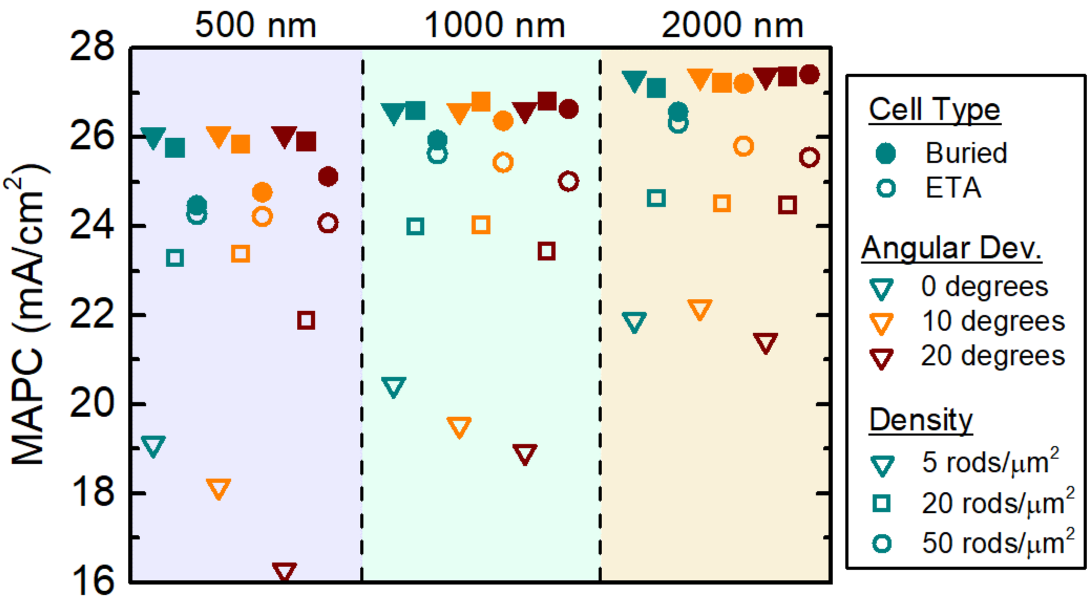

Figure 3.2: The MAPC of ETA and buried CdTe solar cells for different NR geometrical configurations

3.2.1 Haze Analysis of ZnO/CdS NRs

One of the advantages of employing the ZnO NRs coated with the CdS window layer in CdTe solar cells is the high light scattering and light trapping properties obtained by the NRs. The light scattering performance of NRs must be understood to use the NRs with full benefit. For this purpose, the light scattering capabilities of NR structures are quantified with the haze term which refers to the scattered portion of the incident light after passing through the ZnO/CdS NRs. An illustration of haze is shown in Fig. 3.3 for ZnO/CdS NRs. Haze is a wavelength dependent parameter, hence, haze changes throughout the spectrum, and must be examined spectrally. The spectral distribution of haze from ZnO/CdS NRs provides information on light trapping capability and, hence, the absorption in CdTe. However, the haze term is not directly correlated with the absorption in the CdTe and must be examined in caution. Other factors that affect the absorption in CdTe is the total CdTe amount in the solar cell, parasitic absorption in CdS and Au layers, and interference effects occurring in the solar cell, which will be discussed in latter sections. The haze of nanostructured textures depends on the dimensions of the nanostructures such as the height, diameter, density and angular deviation from the vertical axis. In this work, the diameter of the NRs is kept constant and the relation of haze with height, density and angular deviation are investigated.

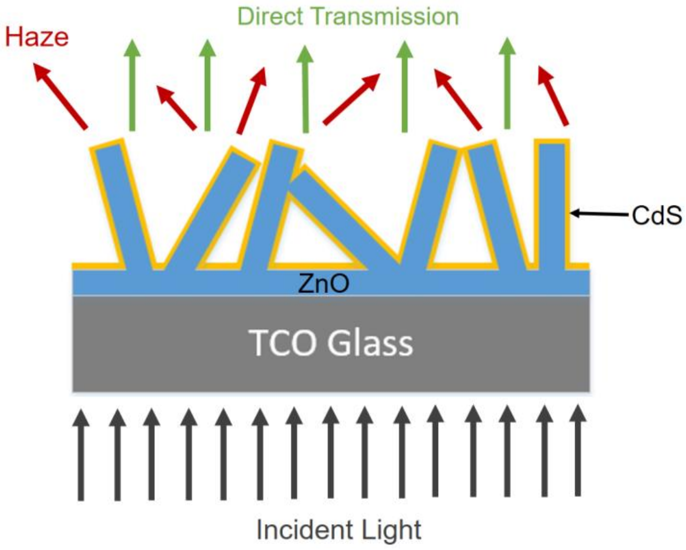

Figure 3.3: An illustration of haze caused by the light to pass through the ZnO/CdS NRs.

The ZnO/CdS NRs were built in the FDTD simulation domain and the structures were optically simulated with the light incident from the glass side. The transmittance of light through TCO layer and the NRs was obtained from the transmittance monitor and the monitor data was used to separate the direct transmittance and haze. The absorption in CdS layer was also obtained from the absorption monitors to investigate the enhanced parasitic absorption in CdS layers with increasing haze. The haze spectra and CdS absorption spectra of various NR geometries are given in Fig. 3.4.

Fig. 3.4.a shows the effect of NR height on the haze and CdS parasitic absorption. There is a ten-fold increase of the haze maximum when 500 nm-tall NRs are made 2000 nm-tall. The large increase in the haze peak shows the potentially better light scattering properties of taller NRs. The haze strength at relatively longer wavelengths are particularly important because the absorption coefficient of CdTe is smaller at longer wavelength, emerging a need for better light scattering. The haze strength at long wavelength is higher for 2000 nm-tall NRs compared to that of 500 nm-tall and 1000 nm-tall NRs, implying a need for taller NRs for an optical absorption enhancement in the CdTe layer. The parasitic absorption in CdS for ZnO/CdS NRs also increases with NR height because stronger haze of NRs enhances the absorption in CdS and for taller NR configurations the CdS amount is higher. High parasitic absorption at short wavelength causes a red-shift of the haze peak.

The NR density provides a significant increase in the haze strength, as shown in Fig. 3.4.b. Although the haze peak is red-shifted due to high parasitic absorption at high NR densities, similar to increasing NR height, the haze strength at relatively long wavelengths is apparently higher. The high parasitic absorption in CdS at high NR densities is similarly attributed to the enhanced haze and CdS amount in the structure.

The increasing angular deviation of the ZnO/CdS NRs increases the haze strength, as seen in Fig. 3.4.c but the parasitic absorption in CdS is not significantly boosted. The peak haze strength increases from 0.05 to 0.2 when angular deviation of NRs is increased from 0 degrees to 20 degrees at 530 nm. The red-shift that was observed increasing NR height and density is not observed for increasing angular deviation because the enhancement of the parasitic absorption in the CdS layer is insignificant compared to the previous cases because the CdS amount in the structure stays the same for constant NR height and density. Therefore, the haze increases at a small cost of parasitic absorption.

In conclusion, haze increases with all three geometrical parameters; the NR height, density, and angular deviation. The enhancement in the parasitic absorption values in the CdS layer in Fig. 3.4 drastically decrease after embedding the CdTe layer due to a better refractive index matching of CdS and CdTe than CdS and air.

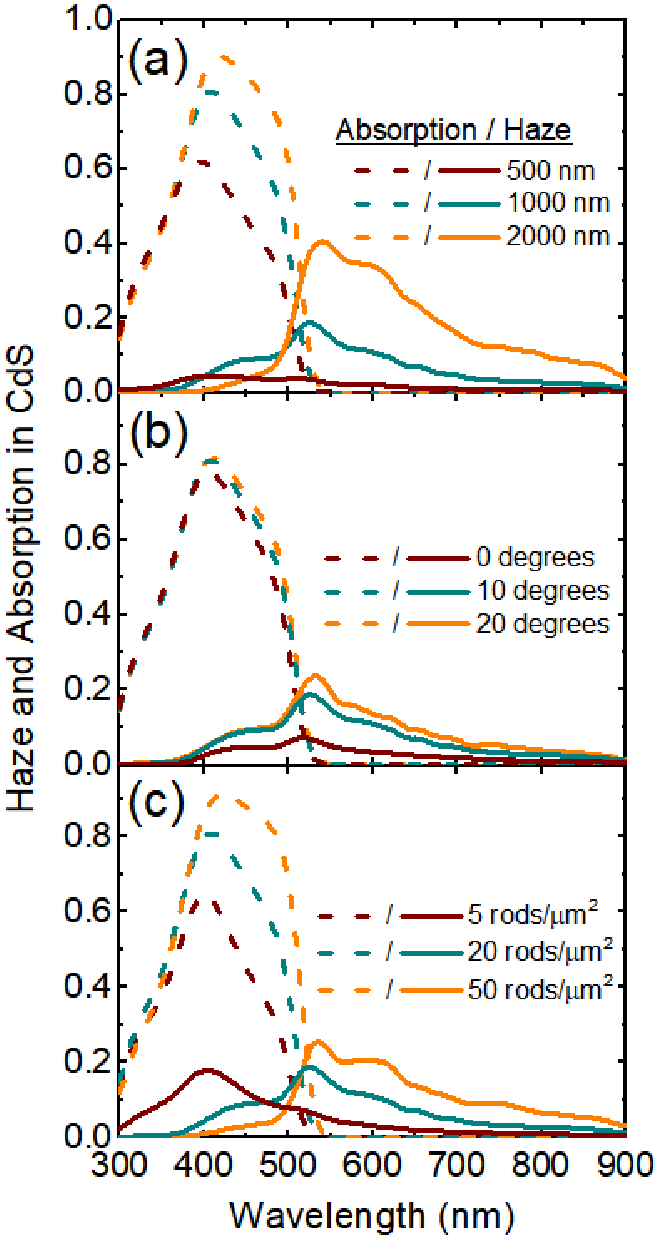

Figure 3.4: The haze and parasitic absorption in CdS with respect to (a) NR height for a density of 20 rods/µm2 and an angular deviation of 10 degrees, (b) NR density for a height of 1000 nm and an angular deviation of 10 degrees, and (c) NR angular deviation for a height of 1000 nm and a density of 20 rods/µm^2

The calculated and measured haze spectra were compared for a structure with ZnO NR height and density of 1400 nm and ~50 rods/μm^2, respectively, as shown in Fig. 3.5. The CdS layer of ZnO/CdS NRs was 20 nm-thick. The simulated and measured haze spectra of both ZnO NRs and ZnO/CdS NRs show a good agreement. Hence, it can be said that the simulation methodology applied for haze is valid.

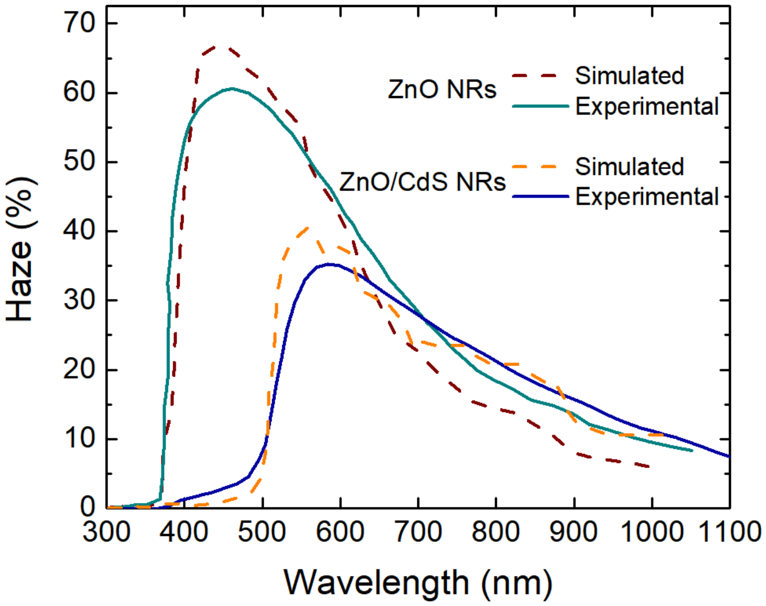

Figure 3.5: Experimental and simulated haze data of ZnO and ZnO/CdS NRs

3.2.2 Equivalent CdTe Thickness Analysis

The evaluation of the optical performance with various geometrical configurations requires the knowledge of the CdTe amount used in the solar cell, besides the haze of the ZnO/CdS NRs. The amount of total CdTe used in a solar cell structure is defined by the equivalent CdTe thickness. Equivalent thickness refers to the thickness of the CdTe layer of a planar CdTe solar cell having the same amount of CdTe material with the nanostructured solar cell. Fig. 3.6 visualizes the equivalent CdTe thickness by showing a nanostructured and a planar solar cell with the same volume of CdTe.

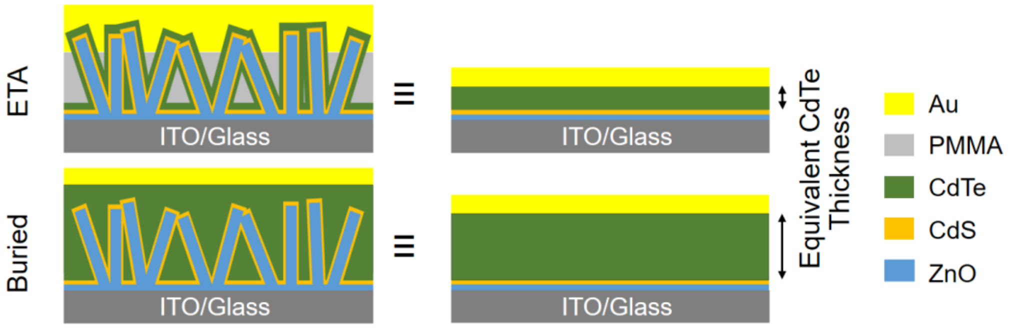

Figure 3.6: Illustration of equivalent CdTe thickness calculation

The geometrical configuration of ZnO NRs directly affects the equivalent CdTe thickness. The change of the equivalent thickness with respect to NR height, density and angular deviation is shown in Fig. 3.7.a, b, and c, respectively. The CdTe equivalent thickness is directly proportional with NR height, as seen in Fig. 3.7.a, since the increasing heights of the NRs increase the height of the solar cell. The NR density, on the other hand, shows the opposite trends for equivalent CdTe thickness of ETA and buried solar cells, as shown in Fig. 3.7.b. For ETA solar cells, higher ZnO NR densities provide larger surface area for the CdTe layer to grow. For the buried solar cells, the increasing ZnO NR density causes a reduction in the total volume of the gaps between ZnO/CdS NRs, leaving less space for the buried CdTe to grow. The resultant equivalent thickness is, hence, decreased. The angular deviation of the NRs, on the other hand, has negligible effect on the CdTe equivalent thickness, as shown in Fig. 3.7.c. For constant heights and densities of NRs, the total area on which CdTe grows is constant, independent of the angular deviation. The slight deviations of the equivalent thickness with angular deviation is caused by the interception of ZnO tips into one another as the angular deviation increases. Although the interception occurs randomly due to the random angular deviation of each NR, the slight variation in the equivalent thickness is insignificant.

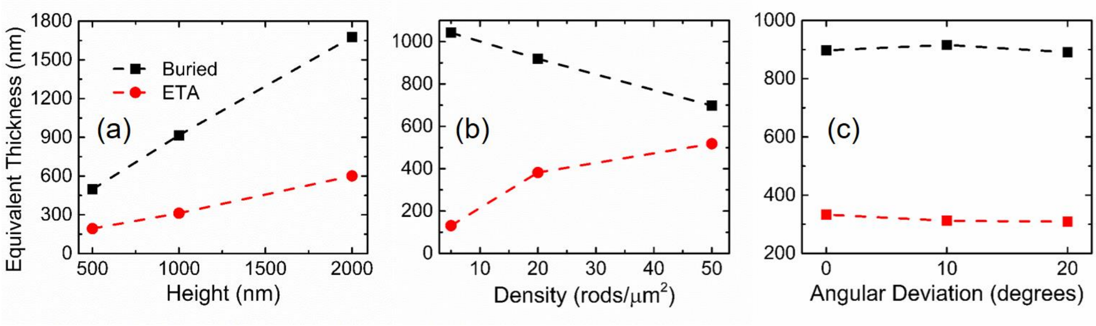

Figure 3.7: The equivalent CdTe with respect to (a) NR height for a density of 20 rods/µm2 and an angular deviation of 10 degrees, (b) NR density for a height of 1000 nm and an angular deviation of 10 degrees, and (c) NR angular deviation for a height of 1000 nm and a density of 20 rods/µm^2.

3.2.3 CdTe Absorption Analysis and Parasitic Losses

In an ideal solar cell, the absorption only takes place within the semiconductor absorber material, which is CdTe in a CdTe solar cell. Any absorption taking place in other layers will have little or no contribution to the photo-current. The parasitic absorption mechanism of the ETA and buried solar cells, therefore, needs to be identified.

The parasitic absorption in Au layer for ETA and buried solar cell structures are shown in Fig. 3.8. For the buried solar cell structure, the parasitic absorption in Au is insignificant with the highest absorption of 3.5 % occurring at 845 nm since the Au layer in a buried solar cell is planar and free of plasmonic effects. The parasitic absorption in Au for the ETA solar cell structure is also shown with a completely Au filled ETA solar cell structure to emphasize the effect of complete Au filling. The ETA solar cells absorb significantly higher than buried solar cells especially at long wavelengths, especially in the completely Au filled case. The high absorption is attributed to the plasmonic effects of the sharp Au edges and the Au surfaces lying in the direction of light propagation in ETA solar cell structure. These sharp edges are formed because of the NRs penetrating into the Au layer but their effects are suppressed by partial PMMA/Au filling which reduces the amount of sharp Au edges. The absorption spectra in Au reveals the relatively high losses in ETA solar cell structure which must be taken into account in the solar cell design procedure.

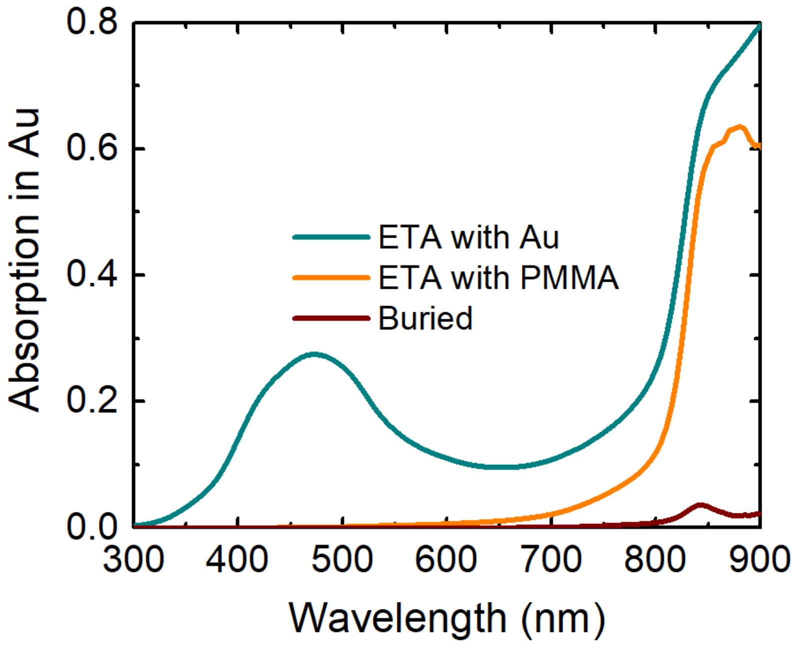

Figure 3.8: The parasitic absorption in the Au layer for 3 solar cell structures with NRs of 1000 nm height, 10 degrees of angular deviation and 20 rods/µm^2 density.

ZnO and CdS have band gaps of 3.3 and 2.4 eV, respectively, corresponding to the energy of photons with 380 and 520 nm wavelengths. Therefore, light with relatively short wavelength faces parasitic absorption in ZnO and CdS. In the haze analysis in section 3.2.1, it was shown that increasing haze of NRs boosted the parasitic absorption in the CdS layer. Although the CdS parasitic absorption decreases drastically after embedding the CdTe layers (will be shown), the parasitic absorption is still a limiting factor when choosing the NR geometry.

The absorption spectra of each layer for 3 ETA and 3 buried solar cell structures are given in Fig. 3.9. The dashed lines indicate the 520 nm wavelength (band gap of CdS) below which the parasitic absorption is high. The absorption in each layer is weighted with the solar spectrum by the Eq. 3.1 and the result is referred to as the weighted absorption. The weighted parasitic absorption of ITO, ZnO and CdS layers are given on the left most side of the graphs while the weighted parasitic absorption in Au is shown on the right most side for ETA solar cells. The weighted absorption in CdTe (can also be called MAPC) is calculated for 300-520 nm and 520-850 nm wavelengths of the spectrum and given on the left-hand side and right-hand side of the dashed lines, respectively. Fig. 3.9.a and b compare the effect of NR height for ETA solar cells with angular deviation and NR density kept constant. The increasing NR height from 500 nm to 2000 nm causes an increase in the weighted parasitic absorption in ITO, ZnO and CdS layers by 0.08 mA/cm^2 and a decrease of 0.04 mA/cm^2 in the weighted absorption of CdTe layer at short wavelengths. For the longer wavelength region than 520 nm, the weighted absorption enhancement in CdTe is 1.17 mA/cm^2 while the weighted absorption in Au decreases from 2.47 to 1.11 mA/cm^2, meaning that the optical advantage at long wavelengths can easily compensate for the losses at short wavelengths. The comparison of Fig. 3.9.b and c reveals effects of NR density on the absorption spectra. An increase in the NR density from 20 to 50 rods/µm^2 causes an increase in the ITO, ZnO and CdS weighted parasitic absorption to 2.0 mA/cm2 and lowers the weighted absorption in CdTe at short wavelengths by 0.1 mA/cm^2. The gain of weighted absorption in CdTe at long wavelength region, however, is 1.33 mA/cm^2 which accounts for the parasitic losses at short wavelengths. One can conclude that absorption in CdTe in ETA solar cells improve significantly with height and NR density.

The buried solar cells show similar trends in terms of weighted parasitic absorption in ITO, ZnO and CdS layers and weighted absorption in CdTe layers with respect to NR height as shown in Fig. 3.9.d and e. The increasing NR height slightly decreases the weighted absorption in CdTe at short wavelengths but the gained weighted absorption at long wavelengths can account for the losses. For NR density, the total weighted absorption in CdTe is 27.22 mA/cm^2 for 20 rods/µm^2 NR density (Fig. 3.9.e) while it is 27.21 mA/cm^2 for 50 rods/µm^2 NR density (Fig. 3.9.f). This result shows that the density variations at 2000 nm-tall NRs do not show an increase in the weighted absorption in CdTe. The variation of MAPC for buried solar cells with respect to NR density for constant angular deviation and NR heights, given in Fig. 3.2, demonstrates that the effect of NR density is dependent on the NR height and angular deviation. Hence, it is concluded that the analysis of haze, equivalent CdTe thickness together with the absorption spectra provided in Fig. 3.9 are required.

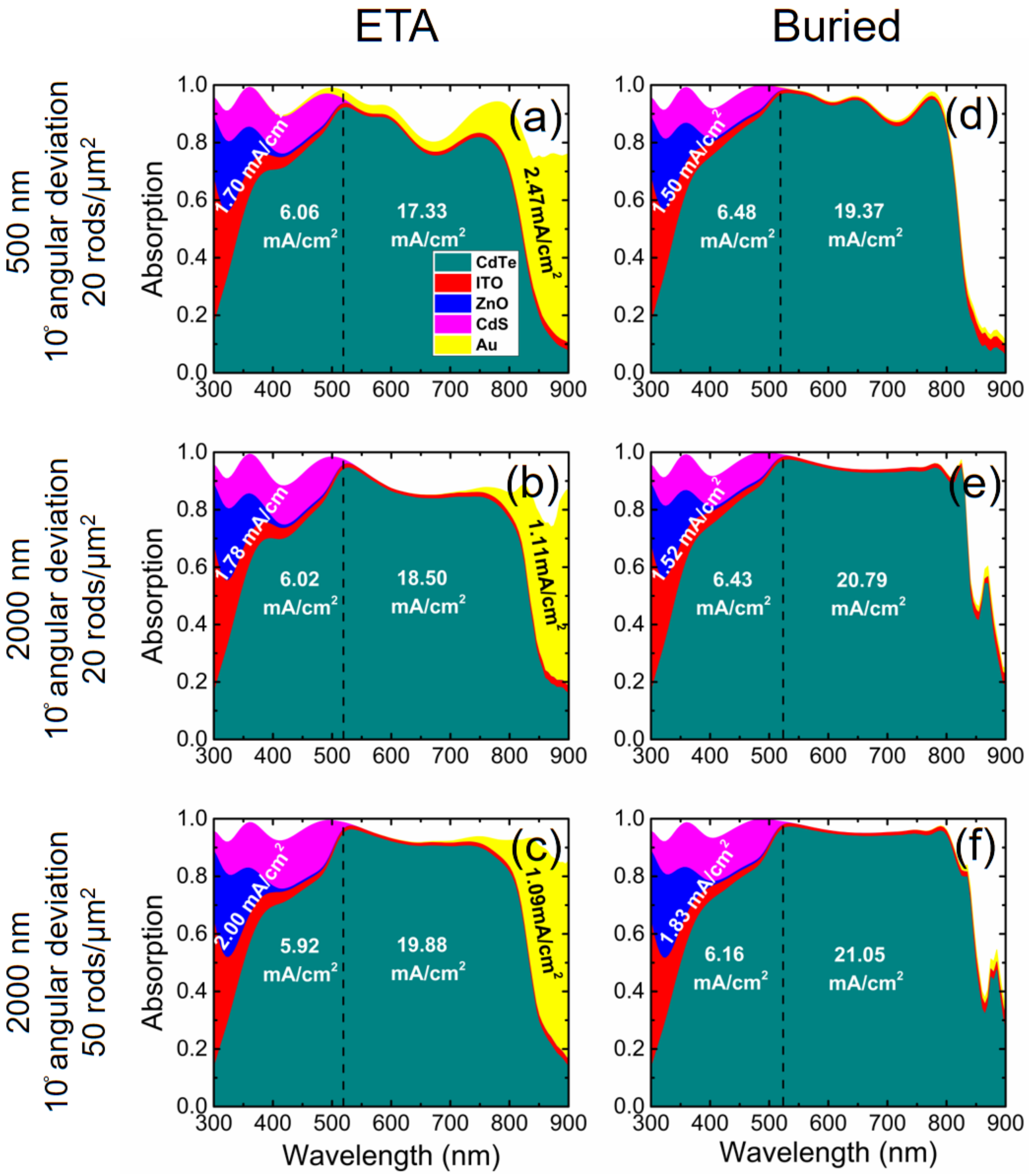

Figure 3.9: The absorption spectra in each layer of ETA and buried solar cells for 3 NR geometrical configurations for each structure.

The photo-generation profiles of the buried solar cells, whose absorption spectra are given in Fig. 3.9.d, e and f, are shown in Fig. 3.10. The absorption in the solar cell with 500 nm-tall NRs and 20 rods/μm^2 density (Fig. 3.10.a) is uniform within the CdTe layer since the solar cell is thin. A closer inspection shows that the photo-generation is larger than 10^{21} cm^{-1} in the CdS layer at the bottom of the solar cell structure and larger than 10^{19} cm^{-1} in the ZnO layer at the bottom of the NRs.

Considering that ZnO and CdS absorb at <520 nm wavelengths, this indicates that most of the parasitic losses occur within tens of nanometers at short wavelengths. For solar cells 2000 nm-tall NRs and 20 rods/μm^2 density (Fig. 3.10.b), the parasitic absorption profile in ZnO and CdS layers are similar to that of the solar cells in Fig. 3.10.a. This result shows the similar values of weighted parasitic absorption shown for 500 and 2000 nm-tall solar cells (Fig. 3.9.c and d). The upper part of the solar cell in Fig. 3.10.b shows the disorderly interference patterns in the photo-generation, which is attributed to the light trapping properties of this solar cell structure. In the solar cell structure with 2000 nm-tall NRs and 50 rods/μm^2 density (Fig. 3.10.c), the strength of the disorderly formed photo-generation at the top parts of the solar cell is stronger than that of the solar cell in Fig. 3.10.b. The enhanced light trapping property is in agreement with the haze spectrum given in Fig. 3.4.b.

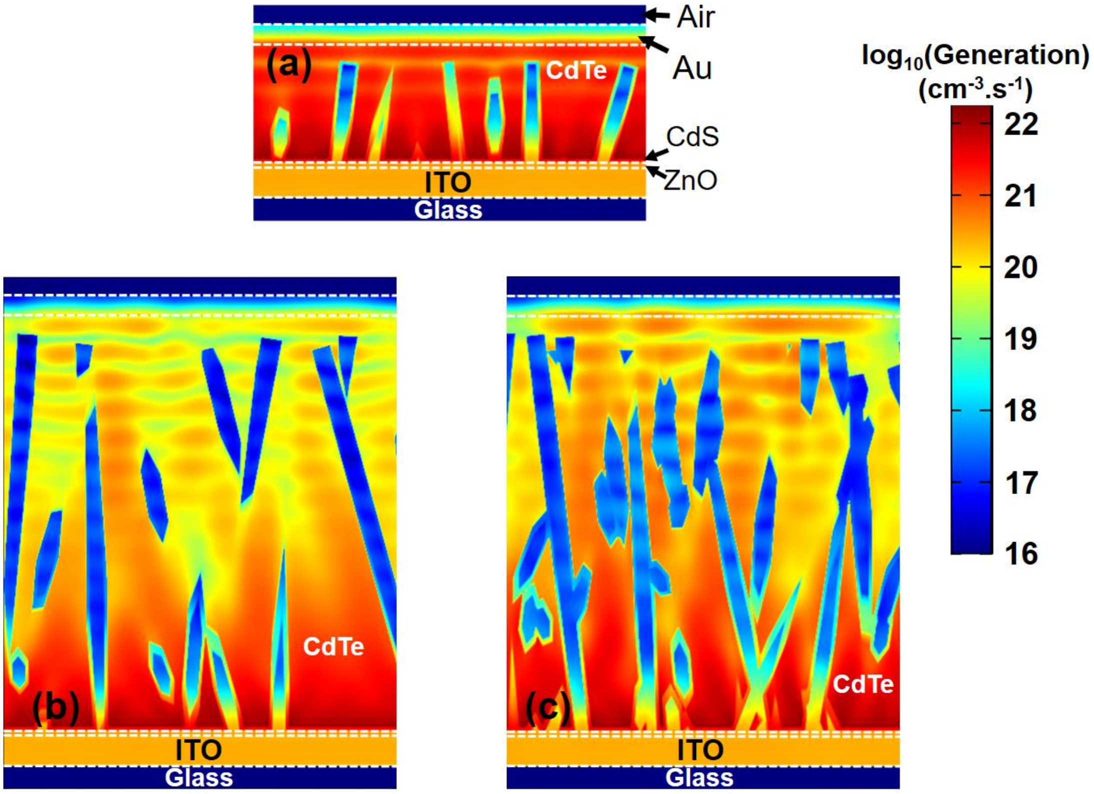

Figure 3.10: Photo-generation profiles of buried solar cells with (a) 500 nm-tall, 10-degree angularly deviated and 20 rods/μm^2 dense NRs, (b) 2000 nm-tall, 10-degree angularly deviated and 20 rods/μm^2 dense NRs and (c) 2000 nm-tall, 10-degree angularly deviated and 50 rods/μm^2 dense NRs.

3.3 Overview of the Optical Performance

3.3.1 ETA CdTe Solar Cells

As it was discussed in section 3.2.1, the haze of the ZnO/CdS NRs increase with all of the three geometrical parameters. The equivalent CdTe thickness also increases with NR height and density, but stays unchanged with angular deviation. Hence, both NR height and density enhance the absorption in CdTe. These findings are confirmed by the trends in Fig. 3.2. The parasitic absorption enhancement in ITO, ZnO and CdS layers with respect to NR height, given by the absorption spectra in Fig. 3.9.a and b, was shown to be relatively unimportant. The parasitic losses with respect to NR density, on the other hand, are compensated for at long wavelengths, as shown in Fig. 3.9.b and c. As a consequence, the MAPC values of ETA solar cells directly increase with NR height and density. Despite the improving absorption in CdTe, one should consider the equivalent CdTe thickness for the comparison of optical performance with the consumed material. Table 3.1 shows the MAPC, equivalent CdTe thickness and the thickness of a planar solar cell with the same MAPC for 5 different ZnO NR geometrical configurations. For 1000 nm-tall ETA solar cells with 10 degrees of angular deviation, the solar cells numbered from 1 to 3, the MAPC steadily increases with NR density at the cost of an equivalent thickness increase from 108 nm to 451 nm. The enhancement factors of these solar cells range from 1.22 to 1.28, indicating a net improvement at material consumption. For the solar cells with 2000 nm-tall and 10 degrees of angular deviation, the solar cells numbered 4 and 5, the MAPC increases with NR density. Although the MAPC values of 2000 nm-tall NRs are slightly higher than their 1000 nm-tall counterparts, the equivalent CdTe thickness of the solar cells with numbers 4 and 5 are 601 and 802 nm, respectively. The enhancement factors of these solar cells, on the other hand, are lower than 1, meaning that a planar solar cell with less CdTe volume can achieve the same MAPC. Hence, the MAPC enhancement in the 2000 nm-tall ETA solar cells due to haze does not account for the increasing equivalent CdTe thickness.

Table 3.1: The MAPC, equivalent CdTe thickness, planar CdTe thickness to achieve the same MAPC and enhancement factor for 5 NR geometrical configurations of ETA solar cells.

Sample	ZnO NR Geometry (Height, Angular Dev., Density)	MAPC (mA/cm^2)	Equivalent CdTe Thickness (nm)	Planar CdTe thickness to achieve the same MAPC (nm)	Enhancement factor
1	1000 nm, 10°, 5 rods/μm^2	19.54	108	138	1.28
2	1000 nm, 10°, 20 rods/μm^2	24.04	312	382	1.22
3	1000 nm, 10°, 50 rods/μm^2	25.44	451	557	1.24
4	2000 nm, 10°, 20 rods/μm^2	24.52	601	404	0.67
5	2000 nm, 10°, 50 rods/μm^2	25.81	802	697	0.87

In conclusion, the performance of ETA solar cells depends more on the CdTe amount than the haze of ZnO/CdS NRs. The ETA solar cells do not efficiently benefit from the light trapping effects of ZnO NRs. Besides, they are disadvantageous at achieving high efficiencies due to the relatively low MAPCs with the highest being less than 26 mA/cm^2.

3.3.2 Buried CdTe Solar Cells

Buried CdTe solar cells achieve higher MAPC than ETA solar cells, seen from Fig. 3.2., which makes them a more preferable candidate for large scale energy production. The MAPCs of the buried solar cells were observed to increase with NR height and angular deviation. The NR density, despite increasing the haze, decreases the equivalent CdTe thickness. Hence, the NR density plays an important role in tuning the equivalent thickness at the cost of haze. The MAPCs, equivalent CdTe thicknesses and planar CdTe thicknesses to achieve the same MAPC of 6 buried CdTe solar cells structures are given in Table 3.2. For the 1st, 2nd and 3rd solar cells with 1000 nm NR height and 10 degrees of angular deviation, the MAPC first slightly increases with an increasing NR density from 5 to 20 rods/μm^2 but decreases with the change from 20 to 50 rods/μm^2. The first increase in MAPC is attributed to the higher haze of 20 rods/μm^2 dense NRs than 5 rods/μm^2 dense NRs despite a reduction in the equivalent CdTe thickness from 1035 nm to 916 nm. However, the solar cell with the NR density of 50 rods/μm^2 fails to compensate for the reduced equivalent CdTe thickness to 641 nm despite the highest haze due to the densest NRs. The MAPCs of the 4th, 5th and 6th solar cells are almost the same despite a reduction in the equivalent CdTe thickness from 1992 nm for the solar cell with 5 rods/μm^2 density down to 1298 nm for the solar cell with 50 rods/μm^2 density. Comparing the 1st, 2nd and 3rd solar cells with 4th, 5th and 6th solar cells, increasing the height of the NRs from 1000 to 2000 nm and the angular deviation from 10 degrees to 20 degrees significantly increases the effectiveness of the used CdTe material. While the enhancement factors of 1st, 2nd and 3rd solar cells are less than 2, the 4th and 5th solar cells have enhancement factors above 2. The 6th solar cell has the record enhancement factor among the investigated solar cell structures with a value of 3.99.

Table 3.2: The MAPC, equivalent CdTe thickness, planar CdTe thickness to achieve the same MAPC and enhancement factor for 6 NR geometrical configurations of buried solar cells.

Sample	ZnO NR Geometry (Height, Angular Dev., Density)	MAPC (mA/cm^2)	Equivalent CdTe Thickness (nm)	Planar CdTe thickness to achieve the same MAPC (nm)	Enhancement factor
1	1000 nm, 10°, 5 rods/μm^2	26.61	1035	1296	1.25
2	1000 nm, 10°, 20 rods/μm^2	26.81	916	1601	1.75
3	1000 nm, 10°, 50 rods/μm^2	26.37	641	1003	1.56
4	2000 nm, 20°, 5 rods/μm^2	27.39	1992	4682	2.35
5	2000 nm, 20°, 50 rods/μm^2	27.36	1702	4041	2.37
6	2000 nm, 20°, 50 rods/μm^2	27.42	1298	5181	3.99

In conclusion, the buried solar cells achieve relatively high MAPCs when tall NR s with high angular deviations are incorporated. While buried solar cells with 1000 and 2000 nm-tall NRs achieve MAPCs of above 26 and 27 mA/cm^2, respectively, the 500 nm-tall NRs perform poor.

3.4 Alternative to the CdS Window Layer

CdS has been used in the CdTe solar cells as the window layer for a long time. However, CdS window layer highly absorbs the light with wavelengths shorter than 520 nm due to its band gap of 2.4 eV. Here, an alternative to the CdS layer is proposed. Mg-doped ZnO layers ($Mg_xZn_{1-x}O$) can serve as window layers. $Mg_xZn_{1-x}O$ has a band gap of nearly 3eV depending on the Mg/Zn ratio. The band gap, electron affinity can be tuned by changing the Mg/Zn ratio. The refractive indices of $Mg_xZn_{1-x}O$ were taken from [57] for x=0.1. To demonstrate the reduction in the parasitic absorption in the window layer, two buried solar cell structure with 20 nm-thick CdS and $Mg_{0.1}Zn_{0.9}O$ layers around 470 nm-tall ZnO NRs were simulated and the photo-generation profiles are given in Fig. 3.11. The thickness of the CdTe layer buried layer in these structures are 830 nm. The structure with the CdS window layer shows relatively high generation within the CdS layer, as seen in Fig. 3.11.a. The solar spectrum weighted absorption in CdS layer is calculated as 2.33 mA/cm^2 while the MAPC of this solar cell structure is 24.64 mA/cm^2. When the $Mg_{0.1}Zn_{0.9}O$ layer is used as the window layer, the generation within the window layer get lower, barely separable from the ZnO buffer layer, as seen in Fig. 3.11.b. The parasitic losses in $Mg_{0.1}Zn_{0.9}O$ layer with this configuration is only 0.25 mA/cm^2, allowing a MAPC of 26.75 mA/cm^2. Hence, the replacement of the window layer with a less absorbing material is optically beneficial to avoid parasitic losses. However, inclusion of $Mg_{0.1}Zn_{0.9}O$ as the window layer in CdTe solar cells is yet to be applied and the Mg/Zn ratios of such structures is to be optimized.

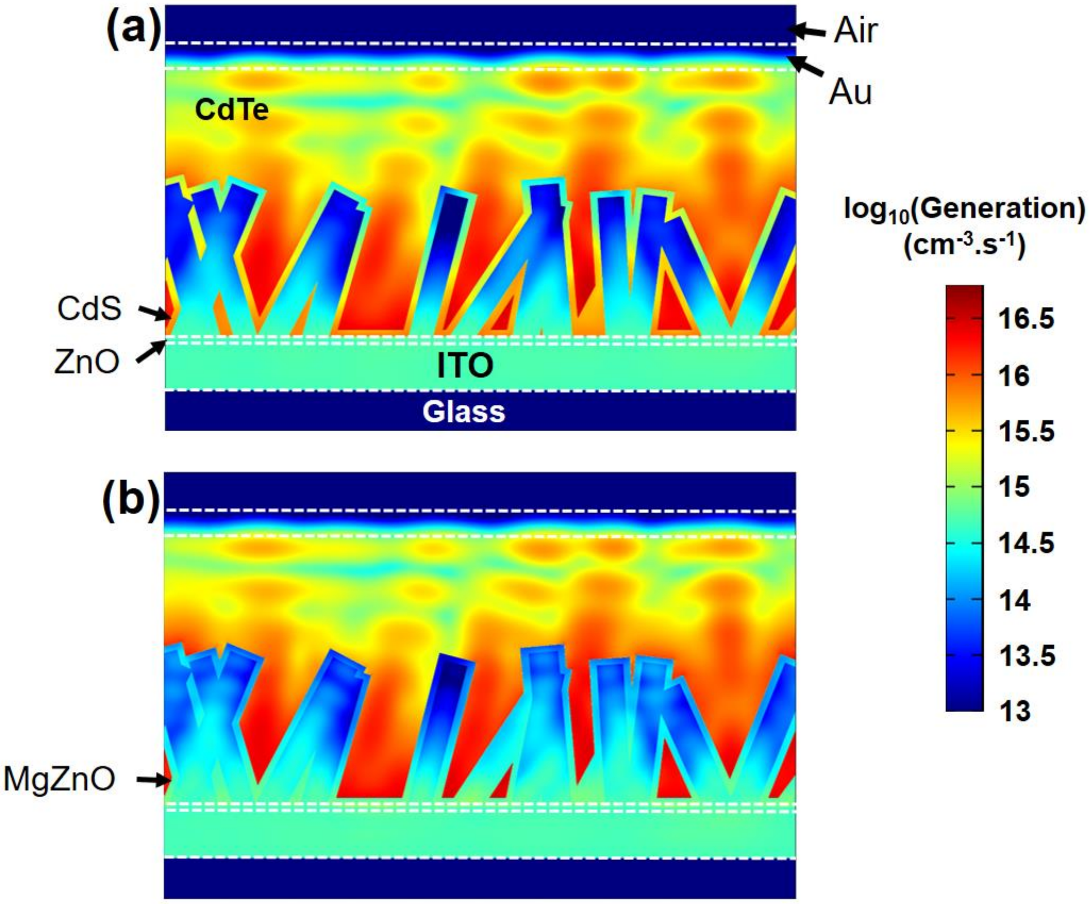

Figure 3.11: The photo-generation profiles of buried CdTe solar cells with (a) 20 nm-thick CdS window layer and (b) 20 nm-thick $Mg_{0.1}Zn_{0.9}O$ layer.

CHAPTER 4

ELECTRICAL OPTIMIZATION OF NANOSTRUCTURED SOLAR CELLS

4.1 Electrical Simulation Methodology

The electrical simulations were performed with Silvaco ATLAS. The simulations were used to obtain collection efficiency and J_{sc} of the solar cell structures. The electrical simulations were done assuming 2-D vertical and periodic ZnO NR structures, unlike the randomly oriented NRs for the optical simulations that were performed in 3-D. The vertical and periodic structure assumption makes the meshing of the structure easy and substantially reduces the computational cost. The oblique and random structures are challenging to be solved with Silvaco ATLAS due to difficulty in meshing and divergence problems when solving the governing equations. While the randomness and angular deviation of ZnO NRs change the optical properties of the solar cell structures, the absence of random and angularly deviated NRs is assumed not to affect the charge collection and J_{sc} of the solar cells. The effect of the changing distance between NRs due to the random orientations of NRs is assumed to average out on the large scale. A similar electrical analysis has been done in a study in which the effect of changing geometries of periodic CdS nanopillars on the CdTe solar cell performance was analyzed [58]. The attention was paid to the changing trends with respect to varying geometrical and material parameters.

The procedure to create and simulate the periodic NR structure from the randomly oriented ZnO NRs is given in Fig. 4.1. Firstly, the average distance between the NRs is found from the density of the random NRs, as shown in Fig. 4.1.a. Then, the 2-D periodic structure is established for ETA (Fig. 4.1.c) and buried (Fig. 4.1.d) CdTe solar cell structures, as seen in Fig. 4.1.b and c, respectively. Then these 2-D structures are built in the optical simulation domain and the photo-generation profiles are obtained. The solar spectrum weighted absorption is calculated in each layer in terms of mA/cm^2 by integrating the solar irradiance with the absorption spectrum of each layer. The optical results of the periodic and vertical structures differ from the random and angularly deviated structures which were discussed in Chapter 3. To compensate for this difference, the photo-generation profile in each layer is linearly scaled with the ratio of solar spectrum weighted absorption of periodic and random NRs. After the scaling, both periodic and random structures give the same solar spectrum weighted absorption. The scaled photo-generation profiles are then fed into the electrical simulations as the input. Then, the simulation is run and the charge collection is solved to obtain J_{sc} of the desired solar cell structures.

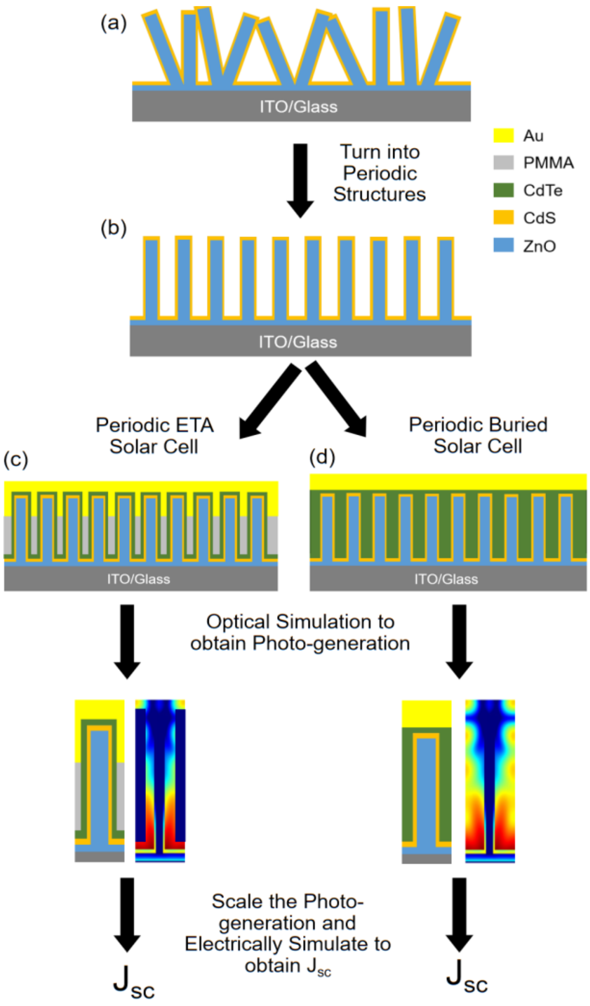

Figure 4.1: An illustration of electrical simulation methodology. (a) The randomly oriented NRs are turned into (b) periodic NRs. The periodic NRs are used to build (c) ETA and (d) buried solar cells. The photo-generation profiles of periodic solar cells are obtained, scaled and fed into electrical simulations to obtain J_{sc}.

4.2 Electrical Simulation Parameters

The material parameters and defect parameters for the electrical simulation were selected from the literature for ITO, ZnO, CdS and CdTe [59]–[63] and given in Table 4.1 and 4.2, respectively. The work functions of both anode and cathode were set to 5.1 eV and the surface recombination velocities for both electrons and holes are set to 10^7 cm/s at anode and cathode interfaces.

Table 4.1: The material properties of CdTe, CdS, ZnO and ITO for electrical simulations.

Parameters	**CdTe**	**CdS**	**ZnO**	**ITO**
Bandgap (eV)	1.45	2.42	3.37	3.65
Electron Affinity (eV)	4.3	4.5	4.5	4.8
Relative dielectric permittivity	9.4	10	9	8.9
Conduction Band effective DOS (cm^{-3})	$7.9x10^{17}$	$2.2x10^{18}$	$2.2x10^{18}$	$5.2x10^{18}$
Valance Band effective DOS (cm^{-3})	$1.3x10^{19}$	$1.8x10^{19}$	$1.8x10^{19}$	$1x10^{18}$
Electron Mobility (cm^2/V.s)	50	100	100	10
Hole Mobility (cm^2/V.s)	20	25	25	10
Doping Type and Density (cm^{-3})	p – 10^{15}-10^{17}	n – 10^{17}	n – 10^{18}	n – 10^{20}

Table 4.2: The defect parameters of CdTe, CdS and ZnO

Parameters	**CdTe**	**CdS**	**ZnO**
Type	Neutral	Neutral	Neutral
E cross section (cm^2)	$1x10^{13}$	$1x10^{17}$	$1x10^{15}$
H cross section (cm^2)	$1x10^{13}$	$1x10^{12}$	$1x10^{12}$
Energetic distribution	Single	Single	Single
Ref. for energy defect	Above E_v	Above E_v	Above E_v
Energy level w.r.t. Reference (eV)	0.725	1.21	1.68
Defect density (cm^{-3})	$1x10^{14}$	$1x10^{18}$	$1x10^{17}$
SRH Lifetime (ns)	10	-	-

The effects of ZnO NR geometry, type of the solar cell (ETA and buried), the p-type doping density of CdTe (N_A) and surface recombination velocity of the CdS/CdTe interface on the J_{sc} of the solar cell structures are analyzed. The ZnO NRs were varied for 3 NR heights (500, 1000 and 2000 nm) and 3 NR densities (5, 20 and 50 rods/μm^2). The ZnO seed layer was kept as 30 nm and CdS layer is kept as 15 nm as in the optical simulations. The ETA and buried solar cells were created for each ZnO NR configurations. N_A was assigned with values of 10^{15}, 10^{16} and 10^{17} cm^{-3} to see the effect of the lowly doped, moderately doped and highly doped CdTe bases. The surface recombination velocities of both electrons and holes between CdS/CdTe interface were changed from 10 cm/s to 10^7 cm/s.

4.3 Electrical Simulation Results

The simulation results of the buried and ETA CdTe solar cells are given in this sub-chapter for different geometrical configurations of ZnO NRs and various doping densities and surface recombination velocities.

4.3.1 Buried Solar Cells

When p-type and n-type semiconductor material contacts, there forms a p-n junction. At the p-side of the material, there exists ionized dopants with negative charges while for the n-side, the ionized dopants with positive charges exist. The charge difference of the two sides create an electric field between the two materials. This electric field opposes to the diffusion of majority charge carriers into the region where they are minority carriers. As a result, the space charge region (SCR) is formed at the vicinity of the two layers. In this study, the n-type material is CdS while the p-type material is CdTe. N-type doping with 1×10^{17} cm^{-3} density was assumed for CdS. Since the CdS doping density is constant, the increasing p-type doping densities in the CdTe reduces the thickness of the SCR in the CdTe region by easily counteracting the field formed in the CdS region due to higher density of ionized dopants. Reducing CdTe doping density, on the other hand, causes the SCR to penetrate deeper into the CdTe layer.

To understand the charge collection mechanism in buried solar cells, the band bending within the CdTe layer with 3 doping densities is presented in Fig. 4.2. The band bending is shown only in the CdTe layer and not in the NRs. The band bending refers to the changing of the conduction band energy with respect to a reference level.

The band structure of CdTe material steeply changes in the SCR. For the doping density of 1x10^{15} cm^{-3}, the SCR penetrates deep into the layer while increasing doping densities reduces the SCR region. For the doping density of 1x10^{17} cm^{-3}, the SCR is confined within a thin shell around the NRs. Adjusting the location of the SCR is crucial since the charge collection depend on it. Ideally, an electron-hole pair created in this region must be collected with a very high efficiency. The electrons are collected from the NRs, while the holes must travel to the rear contacts. Considering that most of the generation occurs close to the front contact, as was shown in Fig. 3.9, the paths of the holes are much longer than that of electrons. In the case of 1x10^{15} cm^{-3} doping density, the holes have to travel a long path from the point they are minority carriers to the point where they become majority carriers. The long path with highly recombinative CdS/CdTe surfaces causes a loss of charges along the way. For high doping densities such as 1x10^{17} cm^{-3}, on the other hand, the holes must only travel a short path until they are collected become majority carriers. For electron, the path length does not significantly change with doping density since the electron-hole pairs are generated close to the NR surface and electrons are efficiently collected in each case. For planar solar cells, unlike the NR-based solar cells, the electron path length also changes with

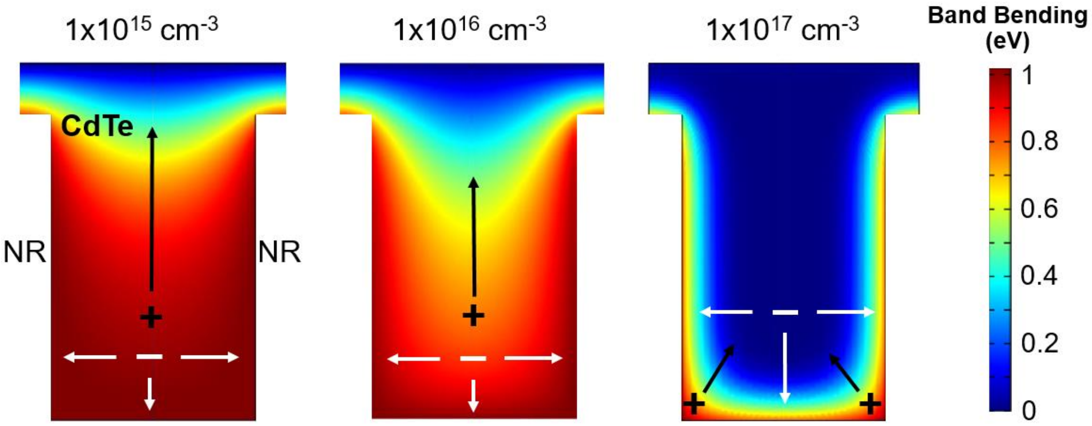

Figure 4.2: Band bending in the CdTe layer for doping densities of 1x10^{15}, 1x10^{16} and 1x10^{17} cm^{-3} for a NR geometry of 500 nm height and 5 rods/µm^{2} density [courtesy of Deniz Türkay]

The J_{sc} of the buried CdTe solar cells are given with respect to CdS/CdTe surface recombination velocity in Fig. 4.3 along with the J_{sc} of the planar solar cells with the same amount of CdTe absorber for comparison. Fig. 4.3.a shows the J_{sc} of the buried solar cells with 2000 nm-tall NR. For 2000 nm-tall NRs, the $1x10^{15}$ cm^{-3} doping density degrades performance resulting in J_{sc} less than 10 mA/cm^2 for all NR densities for the reasons discussed in Fig. 4.2. For 20 rods/μm^2 NR density, a J_{sc} of >27 mA/cm^2 was obtained up to a 10^5 cm/s surface recombination velocity with $1x10^{17}$ cm^{-3} doping density but lower doing densities degraded the performance. For 5 rods/μm^2 NR density, however, even $1x10^{16}$ cm^{-3} doping density can provide a J_{sc} of >27 mA/cm^2 for a surface recombination velocity as high as 10^4 cm/s. Fig. 4.3.b shows the J_{sc} of the solar cells with the same CdTe amount as the solar cells in the Fig. 4.3.a. The highest J_{sc} obtained by using the same material amount is ~23 mA/cm^2 for the $1x10^{15}$ cm^{-3} doping density. The NR-based solar cells outperform their planar counterparts for 5 rods/μm^2 NR density with moderate or high doping density or for 20 rods/μm^2 NR density for 5 rods/μm^2 with high doping density.

The J_{sc} of buried solar cells with 1000 nm-tall NRs are shown in Fig. 4.3.c. The performance of 1000 nm-tall solar cells show a similar trend to that of 2000 nm-tall solar cells by showing a need of 5 or 20 rods/μm^2 NR density. Although 1000 nm-tall solar cells are outperformed by 2000 nm-tall solar cells, they can achieve J_{sc} as high as 26 mA/cm^2 with 5 or 20 rods/μm^2 NR density. Again, $1x10^{16}$ cm^{-3} doping density is sufficient to achieve a high J_{sc} when 5 rods/μm^2 NR density is used. In Fig. 4.3.d, the J_{sc} of the planar solar cells with the same amount of CdTe are shown. The NR-based solar cells can, again, outperform their planar counterparts for 5 rods/μm^2 NR density with moderate or high doping density or for 20 rods/μm^2 NR density for 5 rods/μm^2 with high doping density.

In Fig. 4.3.e, the J_{sc} of the solar cells with 500 nm-tall NRs are shown. The 5 rods/μm^2 NR density shows the highest J_{sc} with a value of 25.5 mA/cm^2 with a doping density of $1x10^{16}$ cm^{-3}. Even a doping density of $1x10^{15}$ cm^{-3} can perform as high as 25 mA/cm^2 provided that the surface recombination velocity stays under 10^3 cm/s. Fig. 4.3.f shows the planar solar cells with the same amount CdTe. In 500 nm-tall NR case, it is seen that, in general, utilization NR-based is not advantageous over planar solar cells.

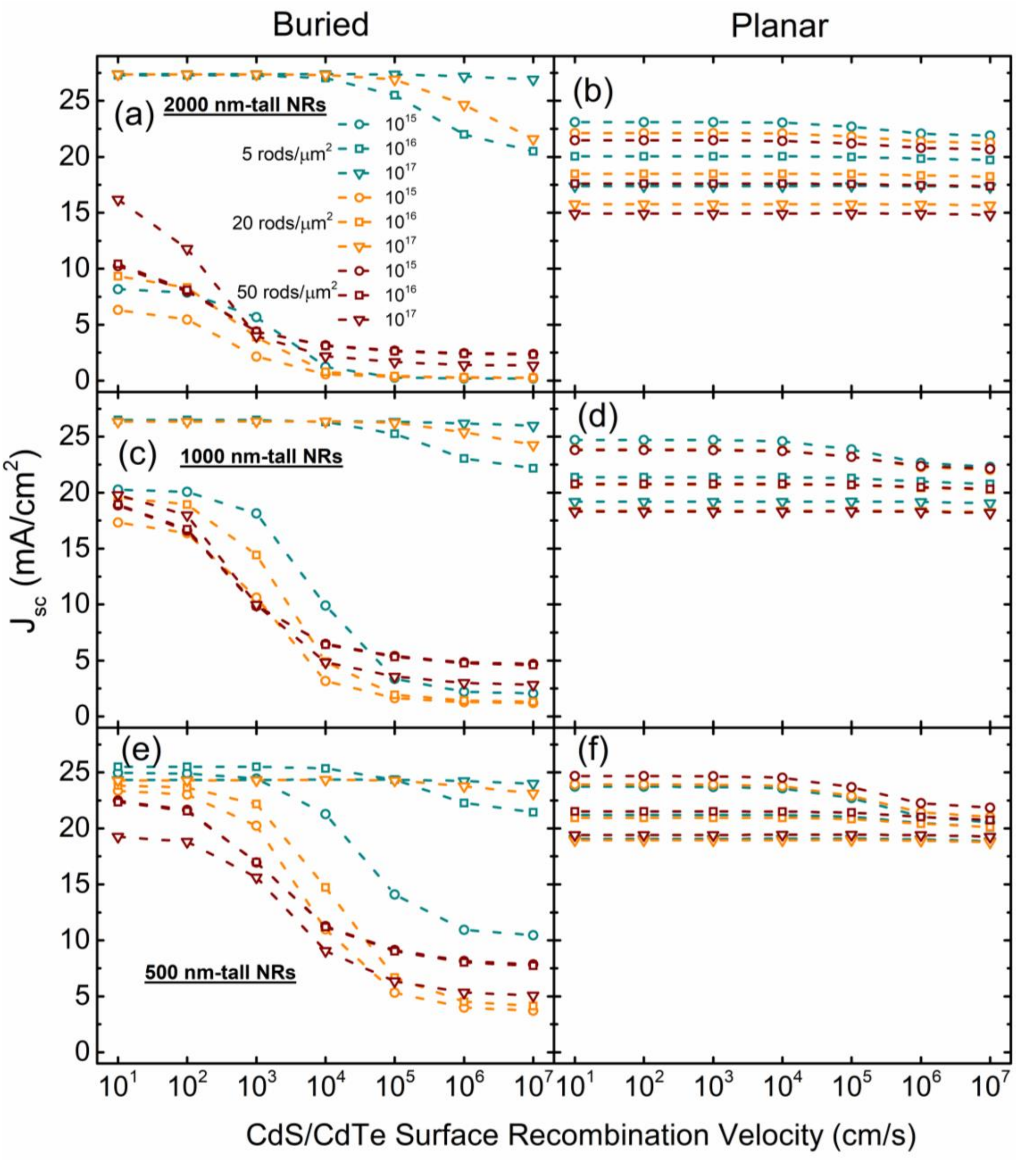

Figure 4.3: The J_{sc} vs. CdS/CdTe surface recombination velocity for buried solar cells with (a) 2000 nm-tall, (c) 1000 nm-tall and (e) 500 nm-tall. The J_{sc} of the planar solar cells with the same amount of CdTe are given corresponding to the (b) 2000 nm-tall, (d) 1000 nm-tall and (f) 500 nm-tall NR cases.

4.3.2 ETA Solar Cells

The charge collection mechanism of the ETA solar cells differs from that of buried solar cells. The discussion given for the band bending of the buried solar cell cannot easily be applied to ETA solar cells because in ETA solar cells the absorber is only 40 nm-thick while in buried solar cells the CdTe bulkier allowing the formation of SCR within the CdTe layer. The high doping density in ETA solar cells increase the hole density within the CdTe layer, increasing the charge collection by reducing the recombination of holes.

The J_{sc} of the ETA solar cells with respect to CdS/CdTe surface recombination velocity are shown in Fig. 4.4. The J_{sc} of the ETA solar cells are lower than that of buried solar cells for all the geometrical configurations. The J_{sc} of ETA solar cells with 2000 nm-tall NRs are seen in Fig. 4.4.a. The J_{sc} values of 2000 nm-tall solar cells suffer if the doping density of $1x10^{15}$ cm^{-3} is not used. This shows that the thin shell of CdTe in ETA solar cells are highly recombinative if the doping density is not high. This is evident from the sharp decrease in the J_{sc} with respect the CdS/CdTe surface recombination velocity. The planar solar cells with same CdTe amount is provided in Fig. 4.4.b. The ETA solar cells are outperformed by the planar solar cells if a very low CdS/CdTe surface recombination velocity is not achieved while maintaining high doping density.

The J_{sc} of 1000-nm tall (Fig. 4.4.c) and 500 nm-tall (Fig. 4.4.e) ETA solar cells show similar trends to that of 2000 nm-tall solar cells. The doping density of $1x10^{17}$ cm^{-3} is required to achieve J_{sc} of 20 mA/cm^2. The sharp decline of J_{sc} with respect to CdS/CdTe surface recombination velocity decreases with decreasing NR height since the path length of holes are short for short NRs. The J_{sc} values of corresponding planar solar cells with the same amount of CdTe, Fig. 4.4.d and f, show that even planar solar cells with doping density of $1x10^{15}$ can outperform the ETA solar cells up to a high CdS/CdTe surface recombination velocity of 10^5 cm/s.

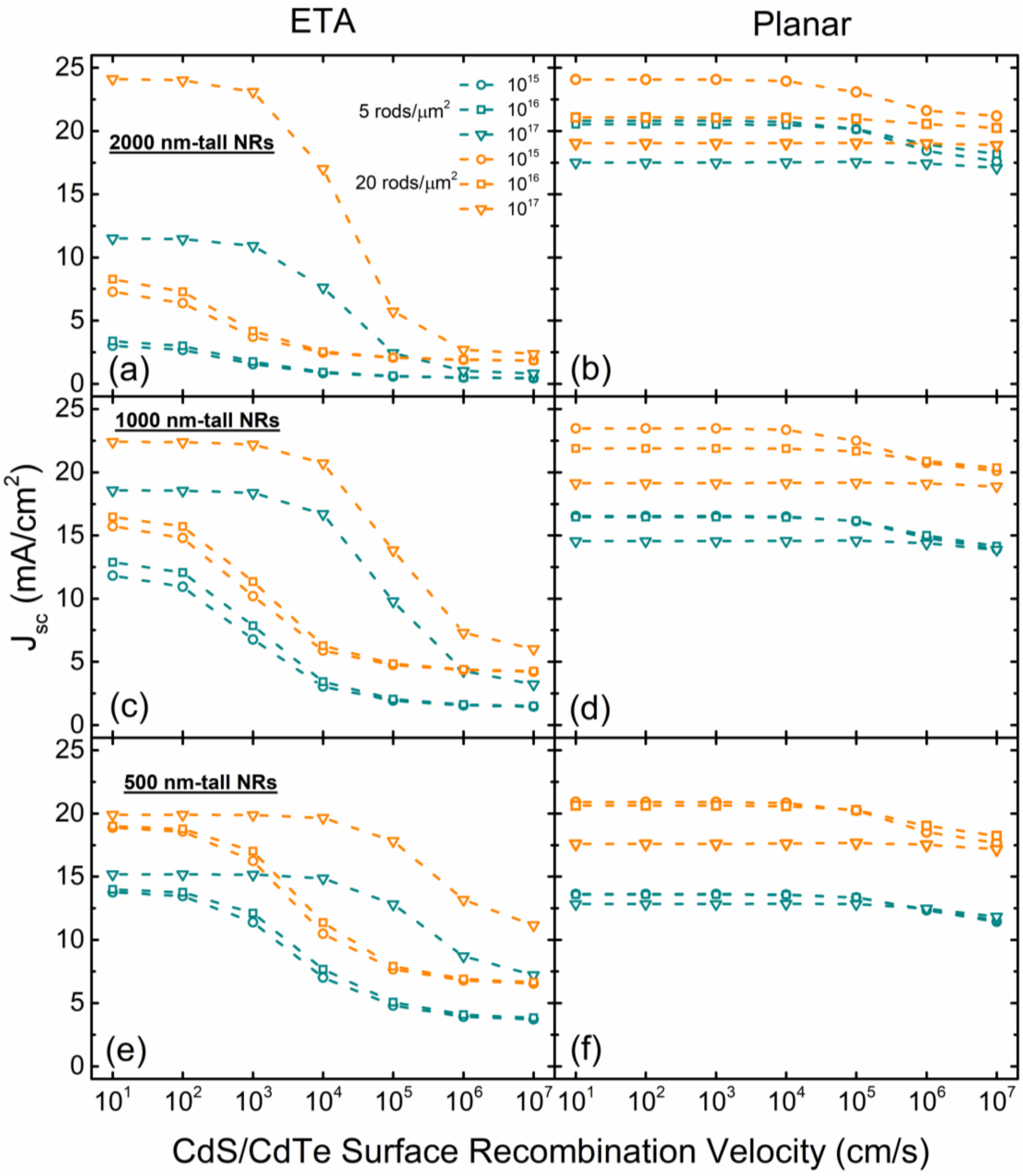

Figure 4.4: The J_{sc} vs. CdS/CdTe surface recombination velocity for ETA solar cells with (a) 2000 nm-tall, (c) 1000 nm-tall and (e) 500 nm-tall. The J_{sc} of the planar solar cells with the same amount of CdTe are given corresponding to the (b) 2000 nm-tall, (d) 1000 nm-tall and (f) 500 nm-tall NR cases

4.4 Overview of the Electrical Performance

The results presented in section 4.3 revealed the superior performance of buried solar cells over ETA solar cells. The downside of ETA solar cells is that the thin CdTe absorber layer is very prone to surface recombination. As a results, very high doping densities and very low CdS/CdTe surface recombination velocities, which are practically difficult to achieve, are required for a successful performance. Even by fulfilling these requirements, the ETA solar cells mostly perform below the planar solar cells with the same amount of CdTe.

The buried solar cells showed promising performances in terms of J_{sc} by outperforming the planar solar cells with moderate doping density and CdS/CdTe surface recombination velocities. The buried solar cells with 1000 nm-tall and 2000 nm-tall NRs, especially with 5 rods/μm^2 NR density, can reach and exceed 27 mA/cm^2 while the planar solar cells with the same amount of CdTe stay below 25 mA/cm^2. However, the NR density of 5 rods/μm^2 refers to the highest consumption of CdTe. The buried solar cell with 2000 nm-tall and 5 rods/μm^2 dense NRs has an equivalent CdTe thickness of 2015 nm. One can reduce the equivalent CdTe thickness for 2000 nm-tall configurations down to 1805 nm by utilizing NR density of 20 rods/μm^2 but this reduction in CdTe amount brings the need for 10^{17} cm^{-3} doping density. Another alternative is to utilize 1000 nm-tall NRs with 5 rods/μm^2, whose equivalent CdTe thickness is around 1050 nm. This configuration allows achieving ~27 mA/cm^2 with 10^{16} cm^{-3} doping density. The equivalent CdTe thickness reduces to 945 nm when a NR density of 2 rods/μm^2 is utilized but this modification requires 10^{17} cm^{-3} doping density.

CHAPTER 5

MATERIAL CHARACTERIZATION OF CDTE LAYERS

5.1 Definition of the Samples

The samples that were characterized in this study were fabricated by at Center for Solar Energy Research (CSER), Swansea University. The characterization techniques were applied to observe the effect of increasing doping densities on the crystal quality of CdTe layer. The applicability of the high doping levels to the CdTe layers, whose necessity was discussed in Chapter 4, were analyzed. The material characterizations were done in facilities of the Center for Solar Energy Research and Application (GÜNAM) in METU, METU Central Laboratory and CSER. The samples contained $CdCl_2$ treated CdTe planar layers with 4 different dopant concentrations on CdZnS window layer on ITO/Glass superstrates. The CdTe and CdZnS layers were deposited by MOCVD and doped during growth. The samples with 4 different dopant concentrations were analyzed to observe the effect of doping on material properties. The CdTe/CdZnS/ITO/glass samples, referred to as the CdTe samples, were doped non-uniformly, hence, the dopant concentration changes with respect to position. The layer structure belongs to the superstrate type CdTe solar cell structure without the rear contact to allow characterization of the rear surface prior to contact metallization. Additional to the CdTe samples, CdZnS samples, which consisted of both as-grown and $CdCl_2$ treated CdZnS layers on ITO/glass superstrates to see the effect of $CdCl_2$ treatment on the CdZnS window layer, were also analyzed. Each characterization technique is given with a brief introduction and the obtained results are discussed. Additional to the planar CdTe characterization, the J-V curves of a NR-based CdTe solar cell device and a planar solar cell device were measured to deduct the efficiencies.

5.2 Material Characterization Techniques

The CdTe and CdZnS samples were characterized by secondary ion mass spectroscopy (SIMS), Raman spectroscopy and scanning electron microscope (SEM) images with an emphasis on CdTe samples. More discussion on CdZnS given in sub-chapter 5.3.

5.2.1 Secondary Ion Mass Spectroscopy

Secondary ion mass spectroscopy is a characterization technique to trace elements in a solid material. An ion beam is incident on the specimen. The ion bombardment causes sputtering of the atoms on the surface of the specimen. The mass/charge ratio of the sputtered atoms are detected and the atom is identified accordingly. The sputtering rate is usually a few nm/sec. Long ion bombardments can be used to obtain information from the deep parts of the specimen [64]. In this part, the As atomic concentration measured with SIMS is given. The SIMS profiling was done through the CdTe layers from rear to front surface of the samples.

The SIMS profiling is done on the CdTe layer starting from the rear CdTe surface, as shown in Fig. 5.1.a. The SIMS profiles are given in Fig. 5.1.b for the 4 different As dopant concentration. The samples are named after the dopant concentrations in the middle parts of the sample where the concentration is almost constant. The sample with $1x10^{16}$ cm^{-3} dopant concentration was intended to be undoped but during the process it was unintentionally doped. The dopant concentration is around the detection level, hence, the As atom concentration fluctuates around $1x10^{16}$ cm^{-3}. The samples with dopant concentrations of $3x10^{17}$ cm^{-3}, $4x10^{18}$ cm^{-3} and $1x10^{19}$ cm^{-3} have high As counts until 300 nm deep from the rear surface. The reason for high dopant concentration at the rear surface is to avoid formation of highly resistive layer near the back contact after solar cell formation. The dopant concentrations of CdTe samples decrease at deeper levels of CdTe, close to the CdZnS window layer. This type of non-uniform dopant concentration is expected to causes a bended band structure to promote easier collection of charge carriers.

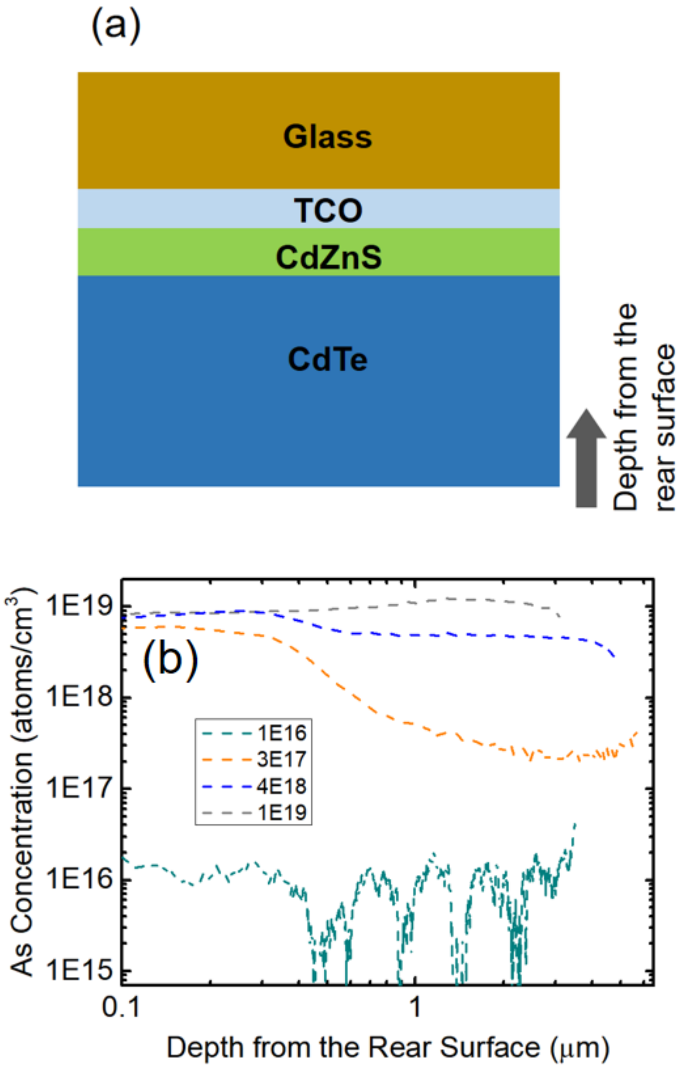

Figure 5.1: The SIMS profile of the CdTe samples

The dopant concentration does not show the active dopants but the As atoms in a given location. The doping density of the CdTe, which was investigated in the electrical analysis, differ from the As atomic concentration in the CdTe films. The information from CSER was that the doping densities of the CdTe films were 7x10^{13} cm^{-3}, 3x10^{14} cm^{-3}, 1x10^{16} cm^{-3} and 2x10^{16} cm^{-3} for the samples with dopant concentrations of 1x10^{16} cm^{-3}, 3x10^{17} cm^{-3}, 4x10^{18} cm^{-3} and 1x10^{19} cm^{-3}, respectively. Therefore, the activation ratio of dopant atoms ranges between 0.1 and 0.3 %. The very low dopant activation ratios cause doping of CdTe to be difficult.

5.2.2 Raman Spectroscopy

Raman spectroscopy is a technique to identify the vibrational and rotational modes in materials [65]. The Raman scattering, first observed by C. V. Raman in 1928, is an inelastic scattering mechanism of photons, as a result the energy of the scattered photons change. The energy change of the Raman scattered photons reveal information about the phonon modes of the material under analysis which are the fingerprints of the material [66]. Usually continuous wave lasers are used for excitation. The reflected light from the material under test goes through a spectrometer and the spectral intensity of the Raman scattered light is observed. The energy shifts of the Raman scattered photons are expressed in terms of wavenumbers (cm^{-1}).

4 CdTe layers with various dopant concentrations on CdZnS/ITO/glass superstrates were characterized with Raman spectroscopy. The peaks in the Raman shift spectrum were identified and compared. Two lasers with 532 and 785 nm wavelengths were used for excitation. Considering the high absorption in CdTe layer at this wavelength, the corresponding absorption depths are 110 and 625 nm for 532 and 785 nm wavelength lasers, respectively. The relatively short absorption depth of 532 nm wavelength in CdTe means the data obtained from this measurement carries information about the shallow region close to the surface of the CdTe layer within a few hundred nanometers. For 785 nm wavelength laser excitation, on the other hand, the light penetrates deeper into the sample and the Raman scattered portion of the light has a higher chance to reach to the detector from the deeper parts of the sample, meaning that the data obtained from these measurements gives information about the deeper parts of the CdTe layers more than 1 µm from the surface.

The Raman spectra of CdTe samples measured from the glass side with 532 nm wavelength laser for different dopant concentrations of $1x10^{16}$ cm^{-3}, $3x10^{17}$ cm^{-3}, $4x10^{18}$ cm^{-3} and $1x10^{19}$ cm^{-3} are given in Fig. 5.2. The broad peaks are due to the photoluminescence of CdZnS around 532 nm wavelength. Photoluminescence is a phenomenon where the electrons in a material are excited from the valance band to the conduction band and during relaxation they give off the excess energy as photons. The energies of the photons are close to the band gap energy of the material, with some deviation from the band gap. The higher energy photons than the band gap are emitted due to the transition occurring from the higher energy states of the conduction band to lower energy states in the valance band. Lower energy photons can be emitted due to the band-tailing (Urbach tails) which causes normally forbidden energy levels within the band gap to be occupied and less energetic photons to be emitted. The different shape of the photoluminescence peak of CdZnS for the sample with 3x10^{17} cm^{-1} shows that the CdZnS properties are slightly different from the other three. The peak at 300 cm^{-1} belongs to CdS phase. The two distinct peaks at round 139 and 165 cm^{-1}, observed for all samples, belong to the transverse optical (TO) mode of Te crystals and LO mode of CdTe, respectively. The Te and CdTe related peaks occur at Raman shifts lower than 200 cm^{-1}, so the emphasis is given in this region.

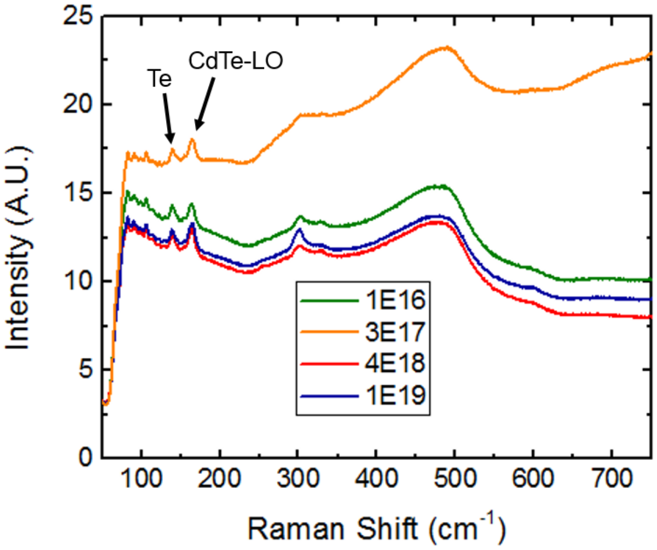

Figure 5.2: The Raman scattering spectrum of CdTe samples excited with 532 nm wavelength from the glass side of the samples

Baseline correction was applied to analyze the peaks at lower than 200 cm^{-1} regions without the effect of photoluminescence peak and the Te and CdTe peaks were fit with a Lorentzian function and are shown in Fig. 5.3. The various dopant concentrations do not cause a significant change in the locations or intensities of Te and CdTe related peaks indicated in Fig. 5.3.a. The full width at half maximum (FWHM) of the Raman peaks give information about the crystallinity of the material. Usually, single crystalline materials show sharp peaks with small FWHM while highly poly-crystalline or amorphous films and highly defective crystals show broad peaks with large FWHM. The dopant concentrations as high as 1x10^{19} cm^{-3} does not significantly change the material quality and crystallinity as can be seen from the FWHM values which change between 7.3 and 8.3 cm^{-1} for Te peak at 139 cm^{-1} and 9.4 and 9.9 cm^{-1} for CdTe peak at 165 cm^{-1}.

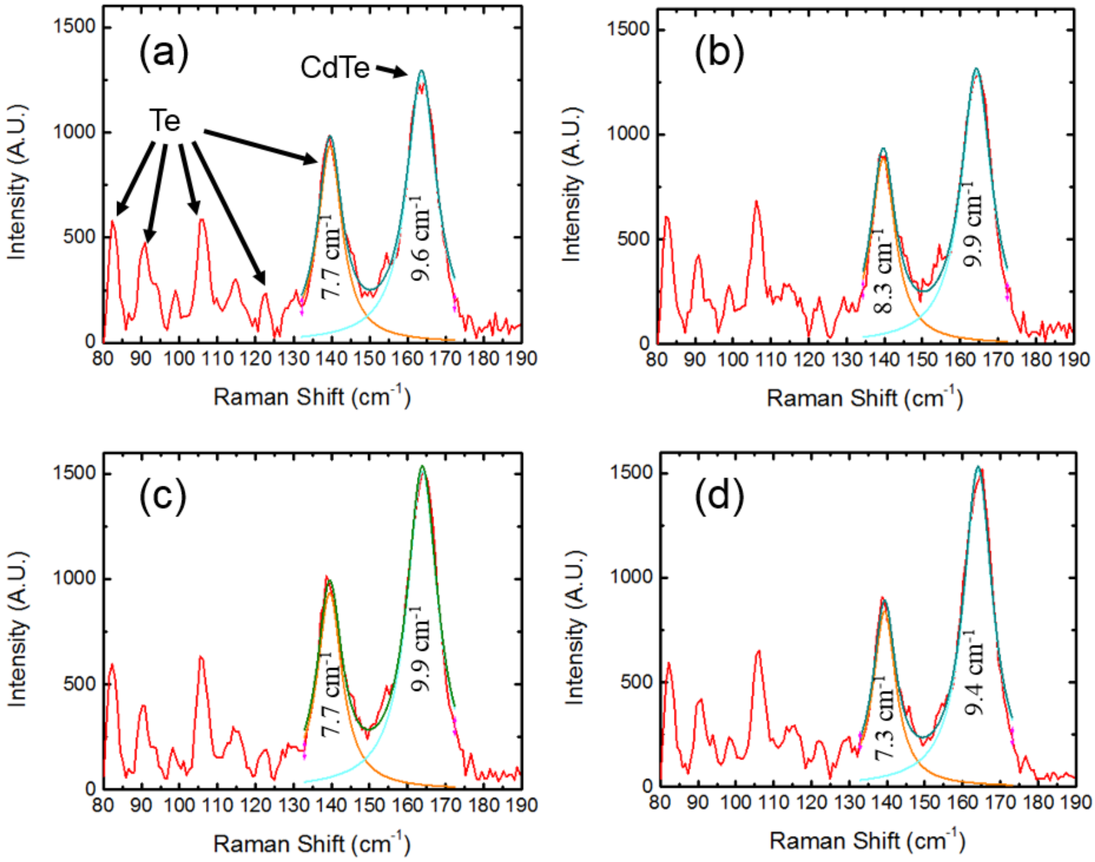

Figure 5.3: The Raman spectra of baseline corrected CdTe samples with dopant concentrations of (a) 10^{16} cm^{-3}, (b) 3*10^{17} cm^{-3}, (c) 4*10^{18} cm^{-3} and (d) 10^{19} cm^{-3}. The FWHM of the main Te and CdTe peaks are shown under the peak.

The apparent Te peaks under each measurements indicates that the CdTe films under investigation are at Te-rich conditions. The main Te peak at 139 cm^{-1} shows the existence of crystalline phase of Te in the CdTe layer. In a previous study, it was shown that dopants in CdTe can replace the defects such as Te antisites in CdTe lattice or Cd vacancies [67], although high dopant concentrations are detrimental since they can create new recombination centers [68]. The ratio peak intensities of CdTe at 169 cm^{-1} with respect to Te at 139 cm^{-1} are given in Fig. 5.4. The CdTe/Te ratio increases with dopant concentration which implies the reduction of crystalline Te phase in the CdTe film. Assuming the reduction of Te is correlated with the Te related defects in the crystal CdTe structure, dopants can reduce the defects in the CdTe layer. The higher dopant concentrations were not observed to degrade the crystal quality, as was discussed for the FWHM values given in Fig. 5.3.

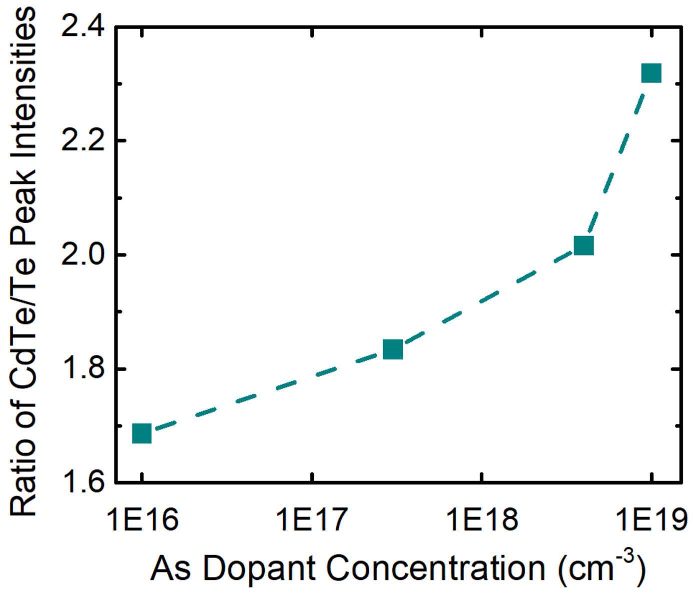

Figure 5.4: The ratio of intensities of the CdTe and Te peaks at 165 cm^{-1} and 139 cm^{-1}, respectively.

The Raman spectra of CdTe samples measured from the rear side (CdTe side) with 785 nm wavelength laser for different dopant concentrations of 10^{16} cm^{-3}, 3x10^{17} cm^{-3}, 4x10^{18} cm^{-3} and 10^{19} cm^{-3} are given in Fig. 5.5. Unlike the excitation with 532 nm wavelength, the Te related peaks were not observed. The main CdTe peak, however, was observed at 167 cm^{-1} except for the sample with dopant concentration of 10^{16} cm^{-3}. For the sample without the CdTe peak, a stronger photoluminescence data was observed.

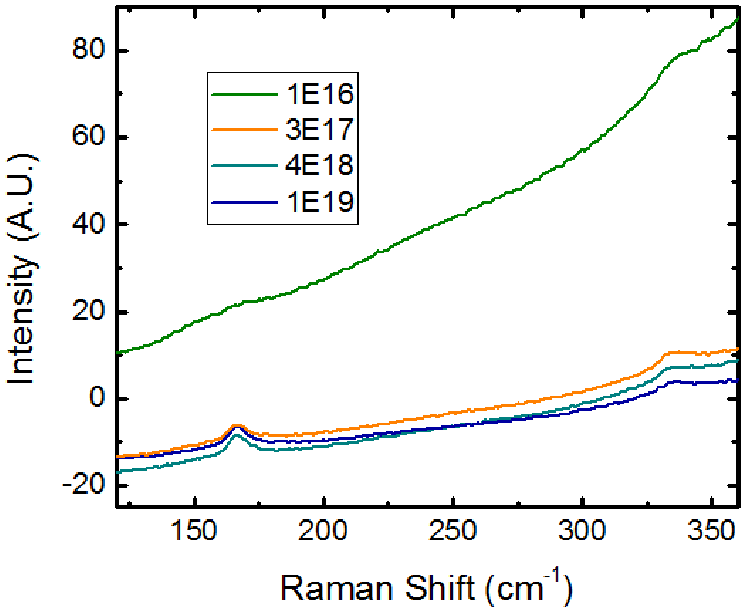

Figure 5.5: Raman spectra of CdTe samples measured from the rear side with 785 nm excitation for (a) 1x10^{16} cm^{-3}, (b) 3x10^{17} cm^{-3}, (c) 4x10^{18} cm^{-3} and (d) 1x10^{19} cm^{-3} dopant concentration.

The baselines of the measured data in Fig. 5.5 were corrected and the FWHM of the observed CdTe peaks were compared in Fig. 5.6. According to the Lorentzian fits on the baseline corrected data, the FWHM value is the smallest for the highest dopant concentration of 1x10^{19} cm^{-3} with a value of 6.9 cm^{-1} as shown in Fig. 5.6.c. This may imply that the high doping does not show a damaging effect on the rear side of the sample. The smaller FWHM of the highly doped sample may be attributed to its more uniform dopant concentration profiles as will be discussed for the SIMS measurements. The samples with dopant concentrations of 3x10^{17} cm^{-3} (Fig. 5.6.a) and 4x10^{18} cm^{-3} (Fig. 5.6.b) showed broader peaks with FWHM of 8.2 and 8.5 cm^{-1}, respectively. Considering the 625 nm absorption depth of the 785 nm wavelength in CdTe, the data plotted in Fig. 5.6 is taken within a 1 µm deep from the rear surface. Hence, the small peak position variations due to the changing dopant concentration may be attributed to the FWHM values observed for the lower doped samples. The absence of Te peaks shows that the Raman scattering mechanism responsible for Te makes the observation of Te peaks difficult, if not impossible, under 785 nm excitation.

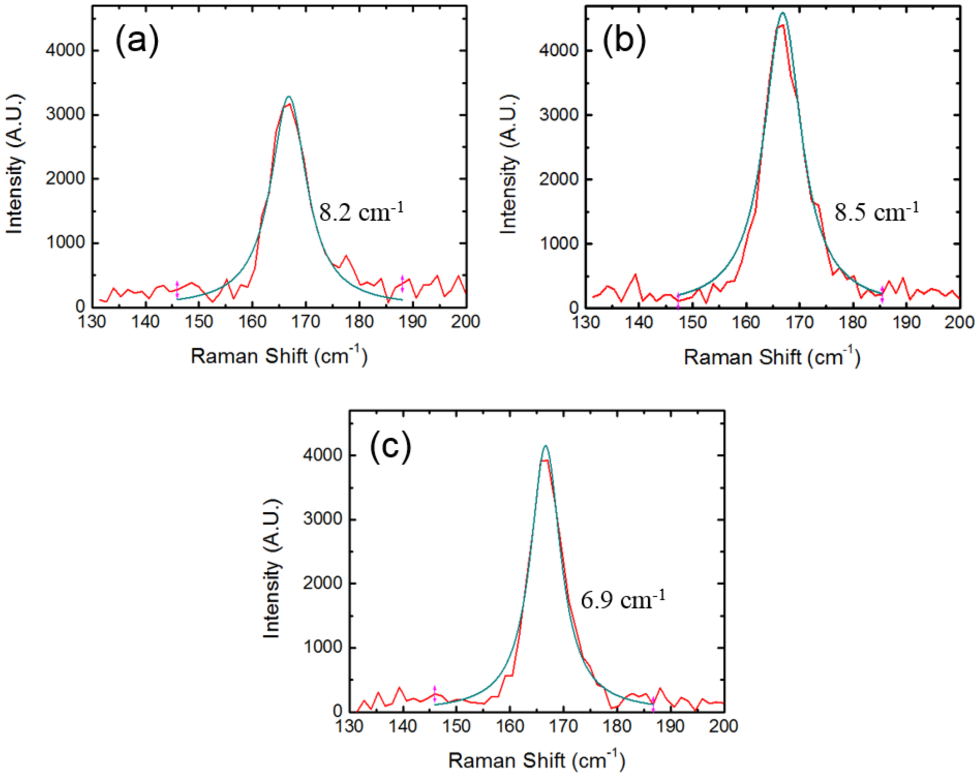

Figure 5.6: The Raman spectra of baseline corrected CdTe samples with dopant concentrations of (a) 3x10^{17} cm^{-3}, (b) 4x10^{18} cm^{-3} and (c) 1x10^{19} cm^{-3} The FWHM of the main CdTe peaks are shown on the right of the peak.

5.2.3 Scanning Electron Microscopy

Scanning electron microscopy (SEM) is a field of electron microscopy that produces images by scanning a focused beam of electron on the surface of a sample and collecting the electrons after they interact with the sample. SEM gives information about the topography of the surface of the sample [69]. In this study, the SEM images of a CdCl$_2$ treated CdZnS/ITO/glass sample and CdTe/CdZnS/ITO/glass samples with 4 different dopant concentrations are observed. The SEM images provide information about the topography of the samples as well as the thicknesses of the planar CdTe layers.

The top view SEM images of the CdTe planar layers on top of CdZnS/ITO/glass are shown in Fig. 5.7 for the 4 samples with different dopant concentrations of 1x10^{16} cm^{-3} (Fig. 5.7.a), 3x10^{17} cm^{-3} (Fig. 5.7.b), 4x10^{18} cm^{-3} (Fig. 5.7.c) and 1x10^{19} cm^{-3} (Fig. 5.7.d). The SEM images show rough surfaces for all of the samples independent of the dopant concentration. The grain sizes of the polycrystalline CdTe layer are around 2 – 4 µm. The roughness and the grains sizes of the CdTe layer are similar in all dopant concentrations, which indicates that high doping concentration does not affect the polycrystalline quality dramatically. It must be noted that the images are from the rear side of the CdTe layer, hence, the structural properties of the CdTe differ significantly from the front side.

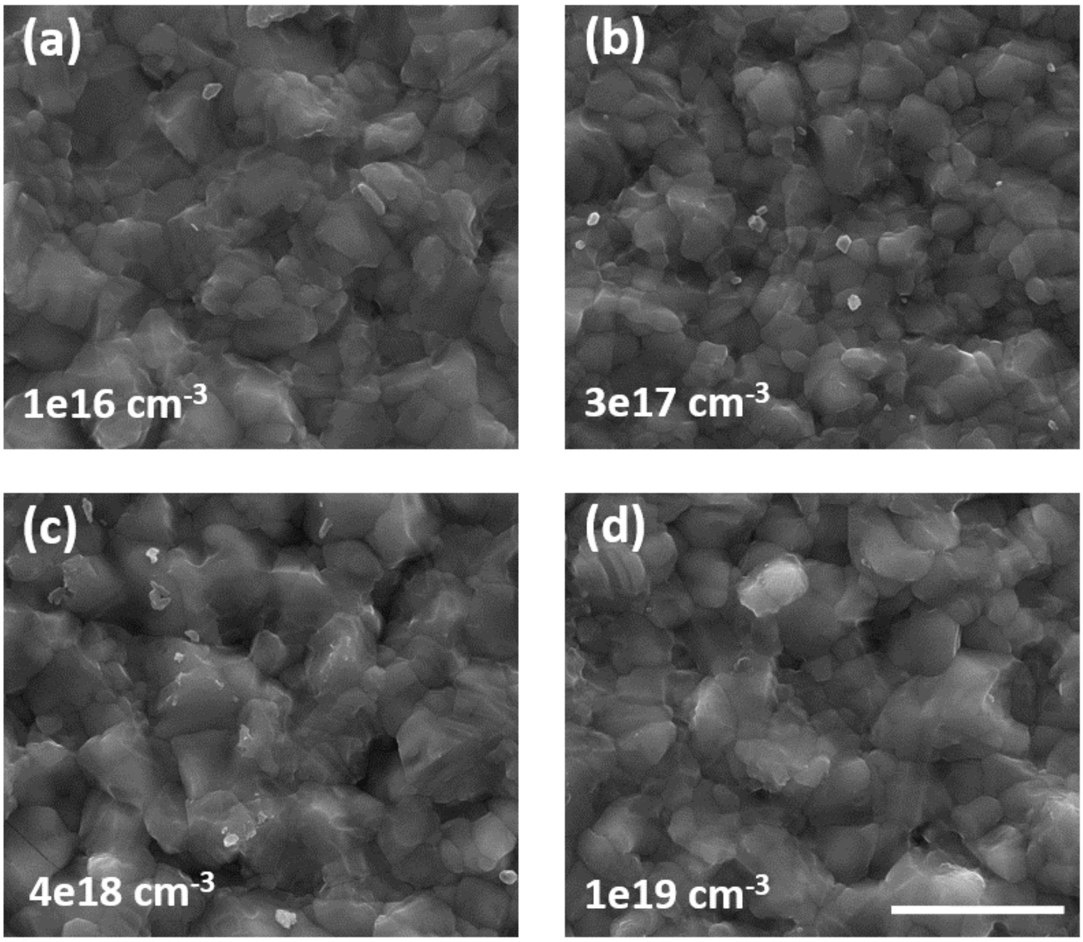

Figure 5.7: The top view SEM images of the 4 CdTe samples on CdZnS/ITO/glass superstrates with different dopant concentrations of (a) 10^{16} cm^{-3}, (b) $3*10^{17}$ cm^{-3}, (c) $4*10^{18}$ cm^{-3} and (d) 10^{19} cm^{-3}. The scale bar is 5 µm.

The cross-sectional view of the SEM images of the CdTe layers are shown in Fig. 5.8 for the 4 samples with different dopant concentrations of $1x10^{16}$ cm^{-3} (Fig. 5.8.a), $3x10^{17}$ cm^{-3} (Fig. 5.8.b), $4x10^{18}$ cm^{-3} (Fig. 5.8.c) and $1x10^{19}$ cm^{-3} (Fig. 5.8.d). The thicknesses of the planar CdTe layers are around 4 µm. The cross-sectional view of the CdTe layers reveal a uniform distribution of CdTe in terms of polycrystalline CdTe quality and thickness. The samples were scribed with a glass cutter and then were broken following the scribe mark. The sides can differ due to the non-uniformities during the breaking process.

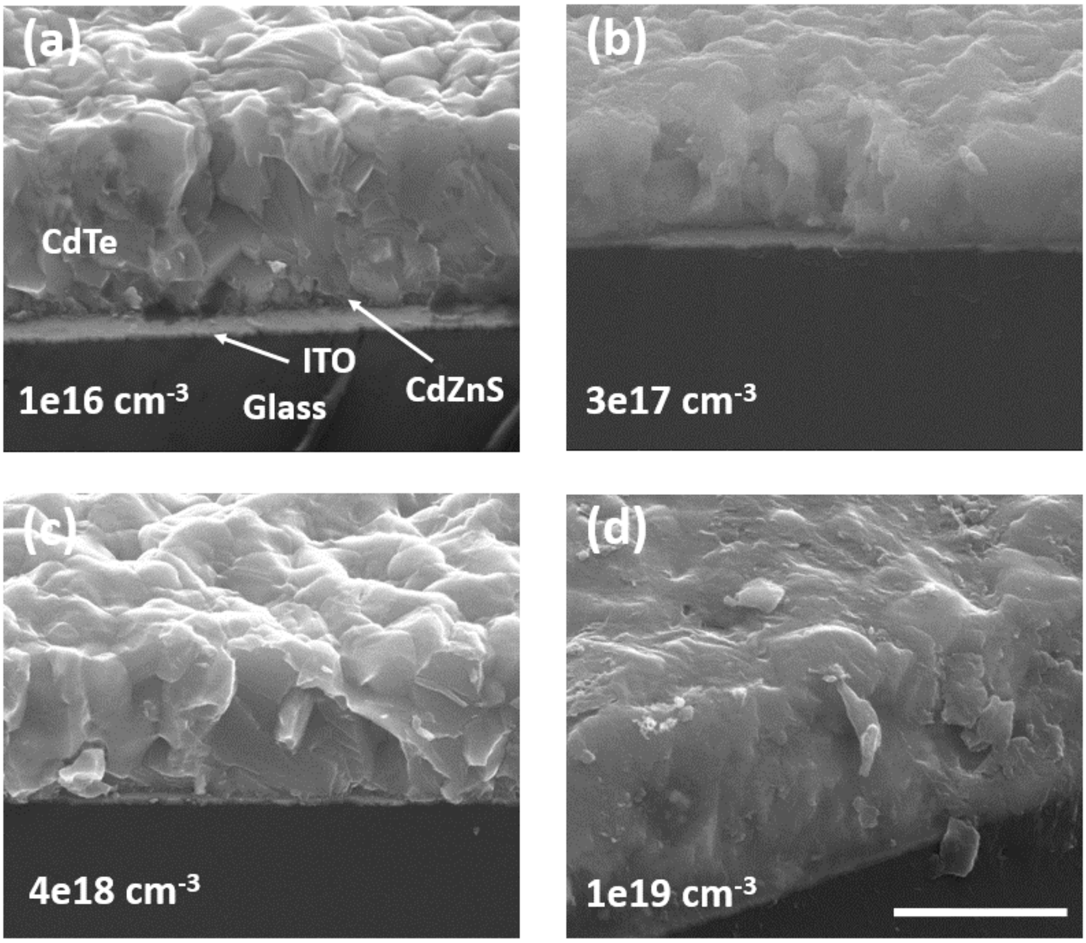

Figure 5.8: The cross-sectional view SEM images of the 4 CdTe samples on CdZnS/ITO/glass superstrates with different dopant concentrations of (a) 10^{16} cm^{-3}, (b) 3*10^{17} cm^{-3}, (c) 4*10^{18} cm^{-3} and (d) 10^{19} cm^{-3}. The scale bar is 5 µm.

5.3 The CdZnS Window Layer

The Raman spectra of the CdZnS/ITO layers with the 532 nm wavelength excitations are given in Fig. 5.9. The as-grown CdZnS/ITO sample shows a sharp Raman peak at ~300 cm^{-1} which corresponds to the first longitudinal optical mode (LO mode) of CdS. The other peak of as-grown sample occurs at 600 cm^{-1} which corresponds to the second LO mode of CdS. No peaks related to ZnS can be observed, probably because the absorption in ZnS at 532 nm wavelength much lower than that of CdS. The $CdCl_2$ treated sample, on the other hand, shows no sharp peaks which indicates that the treatment changes the material properties significantly. A broadened peak around 300 cm^{-1} shows the existence of CdS. It must be noted that the order of the obtained signal for these measurements is more than 10-fold. The much higher signal measured from the treated sample with a broad spectral range indicated that the signal is due to the photoluminescence of the material. The high and broad intensity observed in Fig. 5.9 can be assigned to photoluminescence phenomenon of the CdZnS.

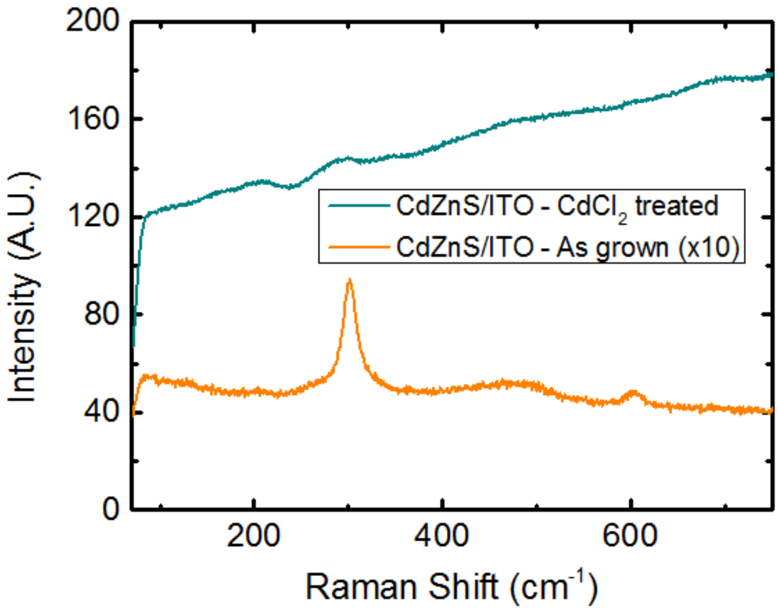

Figure 5.9: The Raman spectra of $CdCl_2$ treated and as-grown (magnified 10 times) CdZnS/ITO samples.

The top view of the CdZnS layer is given in Fig. 5.10. The topography of the surface is rough with small polycrystalline grains with sizes of ~400 nm. The grains show that the material has good crystal quality. The as-grown CdZnS layer on ITO/glass could not be imaged with SEM due to high charging effect usually seen when taking images from insulator layers. This difficulty shows the significant change in the film properties following the $CdCl_2$ treatment.

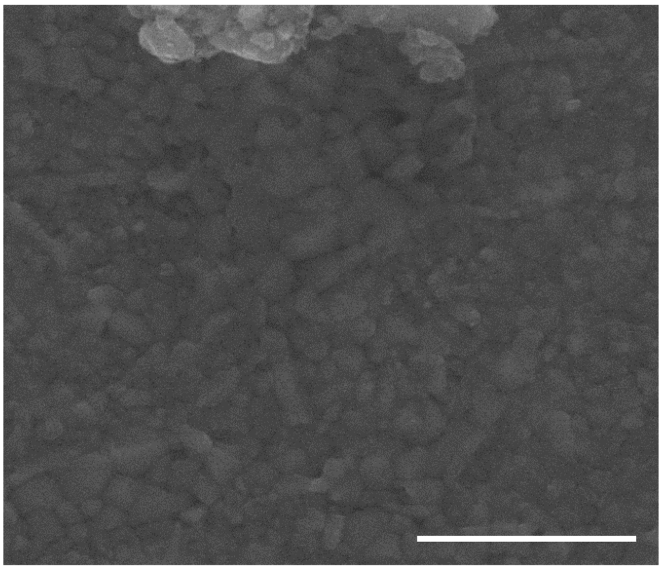

Figure 5.10: The top view SEM image of the $CdCl_2$ treated CdZnS layer on ITO/glass. The scale bar is 2 µm.

The transmission spectra through the CdZnS samples are given in Fig. 5.11 for as-grown and $CdCl_2$ treated CdZnS/ITO film on glass, as-grown CdZnS film on glass and optically simulated CdS/ITO film on glass for comparison. The transmission spectra of the as-grown CdZnS/ITO and CdZnS films are similar; although these two samples transmit less than 60 % of the light below 500 nm they do not show a sharp absorption edge. The interference patterns in the transmission spectra for the two samples change due to the thickness difference of the CdZnS and the existence of the ITO layer in one of the samples. The $CdCl_2$ treated CdZnS/ITO samples, on the other hand, shows a sharp absorption edge around 500 nm wavelength, indicating an existence of a band gap around these energy regions. Such a transmission spectrum is expected from the simulation of CdS/ITO. The similarity of the transmission shows the CdZnS is optically similar to CdS after the $CdCl_2$ treatment and the optical parameters of CdS used in the optical analysis performed in Chapter 3 are in coherence.

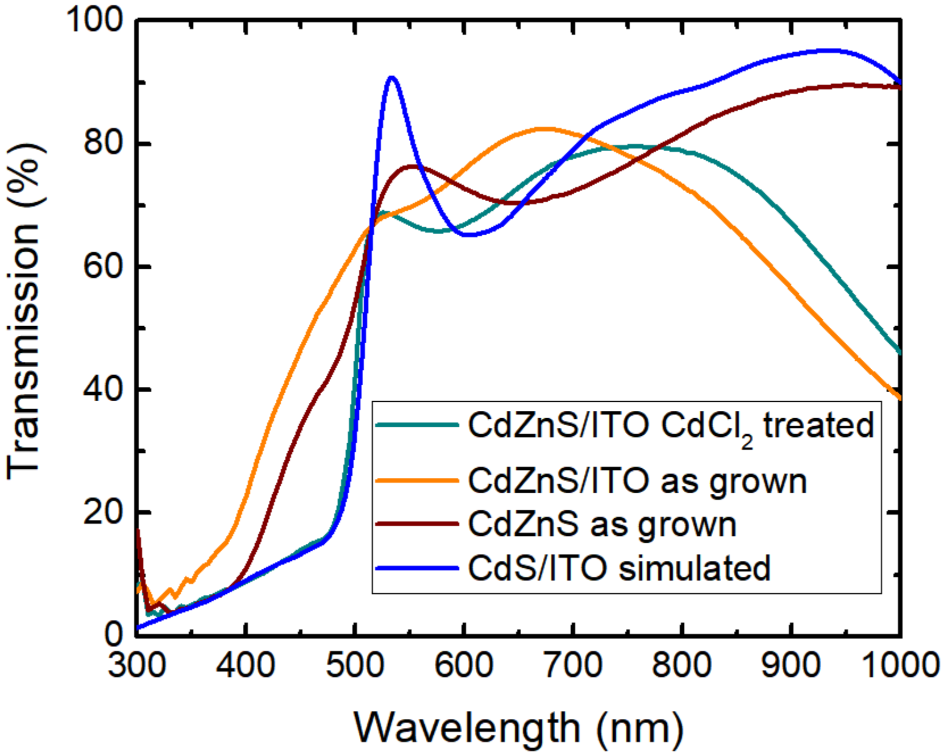

Figure 5.11: Transmission through the as-grown and $CdCl_2$ treated CdZnS/ITO film on glass and as-grown CdZnS film on glass. The light was incident from the CdZnS side and the detection was made from the glass side. Transmission of the optically simulated structure is given for comparison with the experimental data

5.4 Efficiency of NR-based CdTe Solar Cells

The efficiencies NR-based CdTe solar cells and planar CdTe solar cells, fabricated at Swansea University, are discussed in this section. The NR-based CdTe solar cells consisted of 470 nm-tall ZnO NRs with ~90 nm diameters and relatively small angular deviations. The NR density of these solar cells is ~50 rod/µm^2. The CdS thickness around the NRs were measured as 20 nm. The CdTe layer was grown similar to the buried structure, filling the gaps between the NRs, with an excess CdTe layer of around ~300 nm above the NRs. The doping density of these solar cells were not explicitly measured but they are estimated to be around 10^{16} cm^{-3} since the dopant concentrations were expected to be ~10^{19} cm^{-3} from the fabrication parameters. The J-V curves of the NR-based CdTe and planar solar cells are given in Fig. 5.12.a and b, respectively. The NR-based CdTe solar cell achieved an efficiency of 4.26 % while the planar solar cell achieved 4.48 %. While the J_{sc} of 13.8 mA/cm^2 achieved by the

NR-based solar cells, the planar solar cells achieved a J_{sc} of 20.9 mA/cm^2. The lower J_{sc} value of the NR-based solar cell can be attributed to the high density of NRs (~50 rod/µm^2) which was found to require a doping density of 10^{17} cm^{-3}. However, the NR-based solar cell was doped with 10^{16} cm^{-3} density. Therefore, the NR-based solar cell was susceptible to high surface recombination. However, the efficiency of this solar cell is worth noting since it is among the highest efficiencies achieved so far in NR-based CdTe solar cells. [8], [10]–[12].

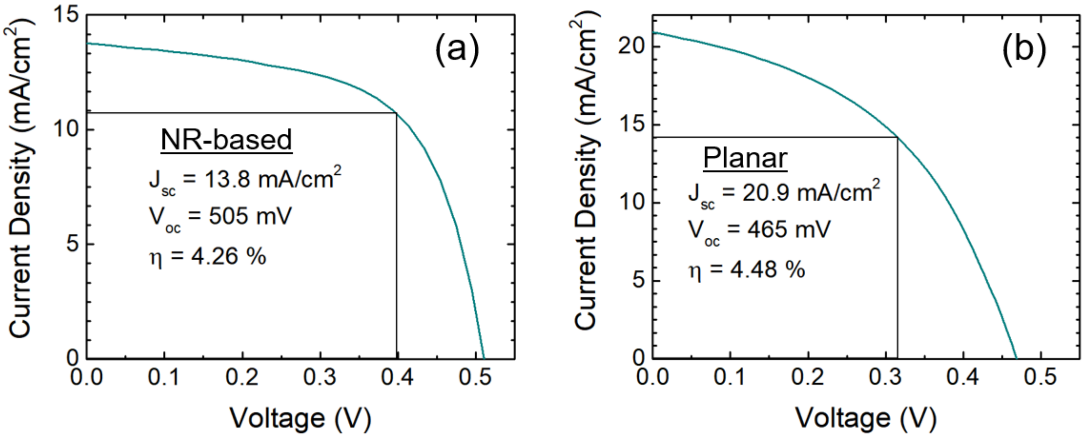

Figure 5.12: The J-V curves of (a) the NR-based CdTe solar cell and (b) the planar CdTe solar cell for comparison

CHAPTER 6

CONCLUSIONS AND OUTLOOK

Solar energy is a valuable source of renewable energy and the expected energy production from the solar is expected to increase thanks to the investment of many countries on solar energy. CdTe is currently the second most used material in the solar energy production with great optical and electrical properties. However, the Te scarcity in the world is a concern and the Te prices are expected to grow. This situation requires decreasing the Te amount in the CdTe solar cells through a reduction in the CdTe material to conserve the attention on CdTe in the solar market. By utilizing traditional planar CdTe solar cell structures, achieving high efficiencies while preserving high efficiencies is difficult due to limited light trapping capabilities of the planar structures and absence of a mechanism aiding the charge collection in the solar cell. Inclusion of ZnO NRs brought new ideas for the novel CdTe solar cells. The NRs enhanced the light trapping in the CdTe absorber layer while keeping the charge collection easy thanks to radial charge collection. Unfortunately, the ZnO NR-based CdTe solar cell technology is immature due to the lack of optimized optical and electrical designs as well as the unrealistic expectations of material properties such as doping and surface recombination velocities.

In this thesis, proposals for the currently low efficiencies of ZnO NR-based CdTe were made by assuming already-achieved material parameters of ZnO, CdS and CdTe layers. The ZnO NR geometries were analyzed and the simulations were performed for appropriate geometries for solar cell structures. Two types of NR-based solar cell structures were proposed, namely the ETA and buried CdTe solar cells. ETA solar cells utilized thin layers of CdTe layers while buried CdTe solar cells utilized a completely buried CdTe between the gaps of ZnO/CdS NRs. The doping densities for the CdTe layers were ranged from easily achievable doping densities such as 10^{15} cm^{-3} up to very demanding doping densities 10^{17} cm^{-3}. The CdS/CdTe surface recombination velocities were also changed from very low values such as 10 cm/s up to 10^7 cm/s to see the degrading effects of the poor interfacial properties, which has been the case for many of the already-achieved ZnO NR-based CdTe solar cells. The effects of the ZnO NR geometries on the CdTe absorption was investigated and the photo-generation profiles obtained from the optical simulations were used in the electrical analysis for a complete understanding of the charge collection performance.

The optical analysis revealed the higher optical performance of buried CdTe solar cells than ETA CdTe solar cells thanks to more efficient use of the CdTe material, as was shown by the enhancement factors. The ETA solar cells showed a strong dependency on the total CdTe amount in the solar cell structure without efficiently benefiting from the light trapping properties of ZnO NRs. ETA solar cells' performance increased with NR height and density but was ambiguous for angular deviation. The MAPC of ETA solar cells remained below 26 mA/cm^2 and the highest calculated J_{sc} was below 25 mA/cm^2 even with the very high doping density of 10^{17} cm^{-3} and the excellent surface recombination velocity of 10 cm/s. As a result, the ETA solar cells were shown to suffer from severe recombination losses due to the long and thin CdTe layer path that the charge carriers must travel before being collected.

The buried CdTe solar cells utilized light scattering and easier charge collection properties of ZnO NRs efficiently, unlike the ETA solar cells, despite the higher amount of CdTe consumption in the solar cell structure. Tall ZnO NRs such as 1000 and 2000 nm with high angular deviations such as 10 and 20 degrees enhance the light trapping in the buried solar cell structure significantly. Changing the NR density helps to optimize the optical performance through a trade-off between the haze and equivalent CdTe thickness. The NR densities of 50 rods/µm^2 with 2µm NR height and 20 degrees of angular deviation can reduce the CdTe amount in the solar cell by 75 % compared to the planar solar cell achieving the same MAPC, however, the electrical performance suffer due to high surface recombination losses for such a dense NR configuration and the J_{sc} is below 25 mA/cm^2 for such a solar cell geometry. For both low and moderate NR densities of 5 and 20 rods/µm^2 with the same height and angular deviation, a 58 % reduction of CdTe was achieved compared to the planar CdTe solar cells while maintaining a high J_{sc} for moderate doping densities and surface recombination velocities. In the 20 rods/µm^2 case, a MAPC of 27.36 was achieved from the optical simulation and a J_{sc} of above 27 mA/cm^2 can be achieved with 10^{17} cm^{-3} doping density. For the 5 rods/µm^2 case, however, J_{sc} of above 27 mA/cm^2 can be achieved even with 10^{16} cm^{-3} doping density and 10^4 cm/s surface recombination velocity. This finding is interesting because the buried solar cell with the ZnO NR configuration of 5 rods/µm^2 density, 2000 nm height and 20 degrees of angular deviation is in a region where a doping density above 10^{16} cm^{-3} and a surface recombination velocity below 10^4 cm/s is not required while achieving a material reduction as high as 58 % compared to the planar cell achieving the same MAPC.

Additional to the simulation studies, various material characterization techniques were performed on the differently doped CdTe planar layers to provide information about the applicability of the proposed material parameters. The scanning electron microscope images showed that the increasing dopant concentration has no noticeable impact on the polycrystalline grain sizes and surface roughness. The Raman spectroscopy measurements have shown the differing material properties on front and rear sides of the CdTe planar layer. The polycrystalline quality of the CdTe layer was not observed to be degraded by the high doping concentrations, showing that the CdTe material properties have been preserved. The recombination lifetimes in the CdTe layers are assumed to not deviate much with the doping density variations. The secondary ion mass spectroscopy measurements have shown the non-uniform dopant concentration through the CdTe layer. The unintentionally doped sample showed a very low dopant concentration of 10^{16} cm^{-3}. The other three samples' dopant concentrations changed throughout the sample but all of them were highly doped with ~10^{19} cm^{-3} near the rear end. This type of doping is supposed to prevent high resistive layer formation at the rear surface which may cause Fermi level pinning.

To conclude, this thesis provided optical and electrical design guidelines for nanostructure-based CdTe solar cells to overcome the relatively low efficiencies achieved for NR based CdTe solar cells. Although the experimental aspect of this work is yet to be studied, the solar cell design path that was provided may guide the scientists towards higher efficiency CdTe solar cells with reduced CdTe amounts.

REFERENCES

[1] Fraunhofer ISE: Photovoltaics Report, updated 19 June 2018.

[2] W. Shockley and H. J. Queisser, “Detailed balance limit of efficiency of p-n junction solar cells,” *J. Appl. Phys.*, vol. 32, no. 3, pp. 510–519, 1961.

[3] S. Shokhovets, O. Ambacher, and G. Gobsch, “Conduction-band dispersion relation and electron effective mass in III-V and II-VI zinc-blende semiconductors,” *Phys. Rev. B - Condens. Matter Mater. Phys.*, vol. 76, no. 12, pp. 1–18, 2007.

[4] M. A. Green, Y. Hishikawa, E. D. Dunlop, D. H. Levi, J. Hohl-Ebinger, and A. W. Y. Ho-Baillie, “Solar cell efficiency tables (version 52),” *Prog. Photovoltaics Res. Appl.*, vol. 26, no. 7, pp. 427–436, 2018.

[5] M. Woodhouse *et al.*, “Perspectives on the pathways for cadmium telluride photovoltaic module manufacturers to address expected increases in the price for tellurium,” *Sol. Energy Mater. Sol. Cells*, vol. 115, pp. 199–212, 2013.

[6] N. Amin, K. Sopian, and M. Konagai, “Numerical modeling of CdS/CdTe and CdS/CdTe/ZnTe solar cells as a function of CdTe thickness,” *Sol. Energy Mater. Sol. Cells*, vol. 91, no. 13, pp. 1202–1208, 2007.

[7] V. Plotnikov, X. Liu, N. Paudel, D. Kwon, K. A. Wieland, and A. D. Compaan, “Thin-film CdTe cells: Reducing the CdTe,” *Thin Solid Films*, vol. 519, no. 21, pp. 7134–7137, 2011.

[8] V. Consonni *et al.*, “Improvement of the physical properties of ZnO/CdTe core-shell nanowire arrays by CdCl2 heat treatment for solar cells,” *Nanoscale Res. Lett.*, vol. 9, no. 1, p. 222, 2014.

[9] X. Cao, P. Chen, and Y. Guo, “Decoration of textured ZnO nanowires array with CdTe quantum dots: Enhanced light-trapping effect and photogenerated charge separation,” *J. Phys. Chem. C*, vol. 112, no. 51, pp. 20560–20566, 2008.

[10] X. Wang *et al.*, “Aligned ZnO/CdTe Core−Shell Nanocable Arrays on Indium Tin Oxide: Synthesis and Photoelectrochemical Properties,” *ACS Nano*, vol. 4, no. 6, pp. 3302–3308, Jun. 2010.

[11] G. Zhang *et al.*, “Improving the photovoltaic performance of solid-state ZnO/CdTe core–shell nanorod array solar cells using a thin CdS interfacial layer,” *J. Mater. Chem. A*, vol. 2, no. 16, pp. 5675–5681, 2014.

[12] M.-J. Jin, X.-Y. Chen, Z.-M. Gao, T. Ling, and X.-W. Du, “Improve photo-electron conversion efficiency of ZnO/CdS coaxial nanorods by p-type CdTe coating,” *Nanotechnology*, vol. 23, no. 48, p. 485401, 2012.

[13] G. Kartopu *et al.*, “Photovoltaic performance of CdS/CdTe junctions on ZnO nanorod arrays,” *Sol. Energy Mater. Sol. Cells*, vol. 176, no. November 2017, pp. 100–108, 2018.

[14] J. D. Major, R. Tena-Zaera, E. Azaceta, and K. Durose, “ZnO nanowire radial CdTe solar cells,” *2015 IEEE 42nd Photovolt. Spec. Conf.*, pp. 1–4, 2015.

[15] O. M. Ten Kate, M. De Jong, H. T. Hintzen, and E. Van Der Kolk, “Efficiency enhancement calculations of state-of-the-art solar cells by luminescent layers with spectral shifting, quantum cutting, and quantum tripling function,” *J. Appl. Phys.*, vol. 114, no. 8, pp. 1–9, 2013.

[16] L. Kranz *et al.*, “Doping of polycrystalline CdTe for high-efficiency solar cells on flexible metal foil,” *Nat. Commun.*, vol. 4, p. 2306, Aug. 2013.

[17] C. Gretener *et al.*, “CdTe/CdS thin film solar cells grown in substrate configuration,” *Prog. Photovoltaics Res. Appl.*, vol. 21, no. 8, pp. 1580–1586, Jun. 2012.

[18] A. Romeo *et al.*, “High-efficiency flexible CdTe solar cells on polymer substrates,” *Sol. Energy Mater. Sol. Cells*, vol. 90, no. 18, pp. 3407–3415, 2006.

[19] B. L. Williams *et al.*, “Challenges and prospects for developing CdS/CdTe substrate solar cells on Mo foils,” *Sol. Energy Mater. Sol. Cells*, vol. 124, pp. 31–38, 2014.

[20] D. Grecu, A. D. Compaan, D. Young, U. Jayamaha, and D. H. Rose, “Photoluminescence of Cu-doped CdTe and related stability issues in CdS/CdTe solar cells,” *J. Appl. Phys.*, vol. 88, no. 5, pp. 2490–2496, 2000.

[21] S. Science, *Encyclopedia of Sustainability Science and Technology*. Springer, 2012.

[22] J. Britt and C. Ferekides, “Thin-film CdS/CdTe solar cell with 15.8% efficiency,” *Appl. Phys. Lett.*, vol. 62, no. 22, pp. 2851–2852, 1993.

[23] T. Nishio *et al.*, “Thin-film CdS/CdTe solar cell with 15.05% efficiency,” in *Photovoltaic Specialists Conference, 1996., Conference Record of the Twenty Fifth IEEE*, 1996, pp. 953–956.

[24] X. Wu, “High-efficiency polycrystalline CdTe thin-film solar cells,” *Sol. Energy*, vol. 77, no. 6, pp. 803–814, 2004.

[25] National Renewable Energy Laboratory, Best Solar Cell Research Efficiencies, retrieved from www.nrel.gov on 20/08/2018.

[26] M. Lee, R. Yang, C. Li, and Z. L. Wang, “Nanowire−Quantum Dot Hybridized Cell for Harvesting Sound and Solar Energies,” *J. Phys. Chem. Lett.*, vol. 1, no. 19, pp. 2929–2935, Oct. 2010.

[27] H. M. Chen *et al.*, “Quantum Dot Monolayer Sensitized ZnO Nanowire-Array Photoelectrodes: True Efficiency for Water Splitting,” *Angew. Chemie Int. Ed.*, vol. 49, no. 34, pp. 5966–5969, Jul. 2010.

[28] B. O’Regan and M. Grätzel, “A low-cost, high-efficiency solar cell based on dye-sensitized colloidal TiO2 films,” *Nature*, vol. 353, p. 737, Oct. 1991.

[29] J. Cui and U. J. Gibson, “A Simple Two-Step Electrodeposition of Cu2O/ZnO

Nanopillar Solar Cells," *J. Phys. Chem. C*, vol. 114, no. 14, pp. 6408–6412, Apr. 2010.

[30] H.-S. Kim *et al.*, "High Efficiency Solid-State Sensitized Solar Cell-Based on Submicrometer Rutile TiO2 Nanorod and CH3NH3PbI3 Perovskite Sensitizer," *Nano Lett.*, vol. 13, no. 6, pp. 2412–2417, Jun. 2013.

[31] J. A. Seabold *et al.*, "Photoelectrochemical Properties of Heterojunction CdTe/TiO $_2$ Electrodes Constructed Using Highly Ordered TiO $_2$ Nanotube Arrays," *Chem. Mater.*, vol. 20, no. 16, pp. 5266–5273, 2008.

[32] X. Gao, H. Li, W. Sun, Q. Chen, F. Tang, and L. Peng, "CdTe Quantum Dots-Sensitized TiO 2 Nanotube Array Photoelectrodes," *J. Phys. Chem. C*, vol. 113, no. April, pp. 7531–7535, 2009.

[33] R. S. Singh, V. K. Rangari, S. Sanagapalli, V. Jayaraman, S. Mahendra, and V. P. Singh, "Nano-structured CdTe, CdS and TiO2for thin film solar cell applications," *Sol. Energy Mater. Sol. Cells*, vol. 82, no. 1–2, pp. 315–330, 2004.

[34] J. Jean *et al.*, "ZnO Nanowire Arrays for Enhanced Photocurrent in PbS Quantum Dot Solar Cells," *Adv. Mater.*, vol. 25, no. 20, pp. 2790–2796, Feb. 2013.

[35] R. Tena-Zaera, J. Elias, and C. Lévy-Clément, "ZnO nanowire arrays: Optical scattering and sensitization to solar light," *Appl. Phys. Lett.*, vol. 93, no. 23, p. 233119, Dec. 2008.

[36] R.-E. Nowak, M. Vehse, O. Sergeev, K. von Maydell, and C. Agert, "ZnO nanorod arrays as light trapping structures in amorphous silicon thin-film solar cells," *Sol. Energy Mater. Sol. Cells*, vol. 125, pp. 305–309, 2014.

[37] Ü. Özgür *et al.*, "A comprehensive review of ZnO materials and devices," *J. Appl. Phys.*, vol. 98, no. 4, p. 41301, Aug. 2005.

[38] A. Rios-Flores, O. Arés, J. M. Camacho, V. Rejon, and J. L. Peña, "Procedure to obtain higher than 14% efficient thin film CdS/CdTe solar cells activated with HCF2Cl gas," *Sol. Energy*, vol. 86, no. 2, pp. 780–785, 2012.

[39] M. C. Akgun, Y. E. Kalay, and H. E. Unalan, "Hydrothermal zinc oxide nanowire growth using zinc acetate dihydrate salt," *J. Mater. Res.*, vol. 27, no. 11, pp. 1445–1451, 2012.

[40] Z. W. Pan, Z. R. Dai, and Z. L. Wang, "Nanobelts of Semiconducting Oxides," *Science (80-.).*, vol. 291, no. 5510, p. 1947 LP-1949, Mar. 2001.

[41] G. She, X. Zhang, W. Shi, X. Fan, and J. C. Chang, "Electrochemical/chemical synthesis of highly-oriented single-crystal ZnO nanotube arrays on transparent conductive substrates," *Electrochem. commun.*, vol. 9, no. 12, pp. 2784–2788, 2007.

[42] F. Li, Y. Ding, P. Gao, X. Xin, and Z. L. Wang, "Single-Crystal Hexagonal Disks and Rings of ZnO: Low-Temperature, Large-Scale Synthesis and Growth

Mechanism," *Angew. Chemie Int. Ed.*, vol. 43, no. 39, pp. 5238–5242, Sep. 2004.

[43] T. Zhang, W. Dong, M. Keeter-Brewer, S. Konar, R. N. Njabon, and Z. R. Tian, "Site-Specific Nucleation and Growth Kinetics in Hierarchical Nanosyntheses of Branched ZnO Crystallites," *J. Am. Chem. Soc.*, vol. 128, no. 33, pp. 10960–10968, Aug. 2006.

[44] A. Belaidi *et al.*, "ZnO-nanorod arrays for solar cells with extremely thin sulfidic absorber," *Sol. Energy Mater. Sol. Cells*, vol. 93, no. 6–7, pp. 1033–1036, 2009.

[45] J. Han *et al.*, "Optimized chemical bath deposited CdS layers for the improvement of CdTe solar cells," *Sol. Energy Mater. Sol. Cells*, vol. 95, no. 3, pp. 816–820, 2011.

[46] D. H. Rose *et al.*, "Fabrication procedures and process sensitivities for CdS/CdTe solar cells," *Prog. Photovoltaics Res. Appl.*, vol. 7, no. 5, pp. 331–340, Oct. 1999.

[47] R. E. T. and A. S.-P. and K. D. and K. H. and S. R. and D. Lane, "Optical Design and Fabrication of Fully Sputtered CdTe/CdS Solar Cells," *J. Phys. Conf. Ser.*, vol. 286, no. 1, p. 12038, 2011.

[48] M. I. Dharmadasa, "Review of the CdCl2 Treatment Used in CdS/CdTe Thin Film Solar Cell Development and New Evidence towards Improved Understanding," *Coatings* , vol. 4, no. 2. 2014.

[49] W. K. Metzger, D. Albin, M. J. Romero, P. Dippo, and M. Young, "CdCl2 treatment, S diffusion, and recombination in polycrystalline CdTe," *J. Appl. Phys.*, vol. 99, no. 10, p. 103703, May 2006.

[50] M. D. G. Potter, D. P. Halliday, M. Cousins, and K. Durose, "A study of the effects of varying cadmium chloride treatment on the luminescent properties of CdTe/CdS thin film solar cells," *Thin Solid Films*, vol. 361–362, pp. 248–252, 2000.

[51] T. Ablekim *et al.*, "Self-compensation in arsenic doping of CdTe," *Sci. Rep.*, vol. 7, no. 1, p. 4563, 2017.

[52] Y. Zhao *et al.*, "Monocrystalline CdTe solar cells with open-circuit voltage over 1 V and efficiency of 17%," *Nat. Energy*, vol. 1, p. 16067, May 2016.

[53] T. A. F. König *et al.*, "Electrically Tunable Plasmonic Behavior of Nanocube–Polymer Nanomaterials Induced by a Redox-Active Electrochromic Polymer," *ACS Nano*, vol. 8, no. 6, pp. 6182–6192, Jun. 2014.

[54] Z. Holman, et al, unpublished data, retrieved from www2.pvlighthouse.com on 17/11/2017.

[55] K. M. McPeak *et al.*, "Plasmonic films can easily be better: Rules and recipes," *ACS Photonics*, vol. 2, no. 3, pp. 326–333, 2015.

[56] I. Bodurov, A. Vlaeva, T. Viraneva, S. Yovcheva, and S. Sainov, “Modified design of a laser refractometer,” *Nanosci. Nanotechnol*, vol. 16, pp. 31–33, 2016.

[57] S. Yang, Y. Liu, Y. Zhang, and D. Mo, “Spectroscopic ellipsometry studies of Mg-doped ZnO thin films prepared by the sol–gel method,” *Phys. status solidi*, vol. 206, no. 7, pp. 1488–1493, Apr. 2009.

[58] R. Kapadia, Z. Fan, and A. Javey, “Design constraints and guidelines for CdS/CdTe nanopillar based photovoltaics,” *Appl. Phys. Lett.*, vol. 96, no. 10, p. 103116, Mar. 2010.

[59] M. Burgelman, P. Nollet, and S. Degrave, “Electronic behaviour of thin-film CdTe solar cells,” *Appl. Phys. A*, vol. 69, no. 2, pp. 149–153, 1999.

[60] M. Gloeckler, A. L. Fahrenbruch, and J. R. Sites, “Numerical modeling of CIGS and CdTe solar cells: setting the baseline,” in *3rd World Conference onPhotovoltaic Energy Conversion, 2003. Proceedings of*, 2003, vol. 1, p. 491–494 Vol.1.

[61] M. Burgelman, P. Nollet, and S. Degrave, “Modelling polycrystalline semiconductor solar cells,” *Thin Solid Films*, vol. 361–362, pp. 527–532, 2000.

[62] T. Minami, T. Miyata, and T. Yamamoto, “Work function of transparent conducting multicomponent oxide thin films prepared by magnetron sputtering,” *Surf. Coatings Technol.*, vol. 108–109, pp. 583–587, 1998.

[63] B. Höffling, A. Schleife, F. Fuchs, C. Rödl, and F. Bechstedt, “Band lineup between silicon and transparent conducting oxides,” *Appl. Phys. Lett.*, vol. 97, no. 3, p. 32116, Jul. 2010.

[64] A. Benninghoven, F. G. Rudenauer, and H. W. Werner, “Secondary Ion Mass Spectrometry: Basic Concepts, Instrumental Aspects, Applications and Trends,” *Int. J.*, 1987.

[65] D. J. Gardiner, P. R. Graves, and W. A. P. Luck, “Practical Raman Spectroscopy,” *Berichte der Bunsengesellschaft für Phys. Chemie*, 1990.

[66] J. R. Ferraro, K. Nakamoto, and C. W. Brown, *Introductory Raman Spectroscopy*. 2003.

[67] T. A. Gessert *et al.*, “Research strategies toward improving thin-film CdTe photovoltaic devices beyond 20% conversion efficiency,” *Sol. Energy Mater. Sol. Cells*, vol. 119, pp. 149–155, 2013.

[68] S. H. Demtsu, D. S. Albin, J. R. Sites, W. K. Metzger, and A. Duda, “Cu-related recombination in CdS/CdTe solar cells,” *Thin Solid Films*, vol. 516, no. 8, pp. 2251–2254, 2008.

[69] D. J. Stokes, *Principles and Practice of Variable Pressure/Environmental Scanning Electron Microscopy (VP-ESEM)*. 2008.